

## The Spectrometer/Telescope for Imaging X-rays (STIX)

Säm Krucker<sup>1,2</sup>, G. J. Hurford<sup>1,2</sup>, O. Grimm<sup>1,3</sup>, S. Kögl<sup>1</sup>, H.-P Gröbelbauer<sup>1</sup>, L. Etesi<sup>1</sup>, D. Casadei<sup>1</sup>, A. Csillaghy<sup>1</sup>, A. O. Benz<sup>1</sup>, N. G. Arnold<sup>1</sup>, F. Molendini<sup>1</sup>, P. Orleanski<sup>1</sup>, D. Schori<sup>1</sup>, H. Xiao<sup>1</sup>, M. Kuhar<sup>1</sup>, N. Hochmuth<sup>1</sup>, S. Felix<sup>1</sup>, F. Schramka<sup>1</sup>, S. Marcin<sup>1</sup>, S. Kobler<sup>1</sup>, L. Iseli<sup>1</sup>, M. Dreier<sup>1</sup>, H. J. Wiehl<sup>1</sup>, L. Kleint<sup>1</sup>, M. Battaglia<sup>1</sup>, E. Lastufka<sup>1,3</sup>, H. Sathiapal<sup>1</sup>, K. Lapadula<sup>1</sup>, M. Bednarzik<sup>4</sup>, G. Birrer<sup>4</sup>, St. Stutz<sup>4</sup>, Ch. Wild<sup>4</sup>, F. Marone<sup>4</sup>, K. R. Skup<sup>5</sup>, A. Cichocki<sup>5</sup>, K. Ber<sup>5</sup>, K. Rutkowski<sup>5</sup>, W. Bujwan<sup>5</sup>, G. Juchnikowski<sup>5</sup>, M. Winkler<sup>5</sup>, M. Darmetko<sup>5</sup>, M. Michalska<sup>5</sup>, K. Seweryn<sup>5</sup>, A. Białek<sup>5</sup>, P. Osica<sup>5</sup>, J. Sylwester<sup>5</sup>, M. Kowalinski<sup>5</sup>, D. Ścisłowski<sup>5</sup>, M. Siarkowski<sup>5</sup>, M. Stęslicki<sup>5</sup>, T. Mrozek<sup>6,5</sup>, P. Podgórska<sup>5</sup>, A. Meuris<sup>7</sup>, O. Limousin<sup>7</sup>, O. Gevin<sup>8</sup>, I. Le Mer<sup>7</sup>, S. Brun<sup>7</sup>, A. Strugarek<sup>7</sup>, N. Vilmer<sup>9</sup>, S. Musset<sup>9,10</sup>, M. Maksimović<sup>9</sup>, F. Fárník<sup>11</sup>, Z. Kozáček<sup>11</sup>, J. Kašparová<sup>11</sup>, G. Mann<sup>12</sup>, H. Önel<sup>12</sup>, A. Warmuth<sup>12</sup>, J. Rendtel<sup>12</sup>, J. Anderson<sup>12</sup>, S. Bauer<sup>12</sup>, F. Dionies<sup>12</sup>, J. Paschke<sup>12</sup>, D. Plüschke<sup>12</sup>, M. Woche<sup>12</sup>, F. Schuller<sup>12</sup>, A. M. Veronig<sup>13</sup>, E. C. M. Dickson<sup>13</sup>, P. T. Gallagher<sup>14,15</sup>, S. A. Maloney<sup>15,14</sup>, D. S. Bloomfield<sup>14,16</sup>, M. Piana<sup>17</sup>, A. M. Massone<sup>17</sup>, F. Benvenuto<sup>17</sup>, P. Massa<sup>17</sup>, R. A. Schwartz<sup>13,14,18</sup>, B. R. Dennis<sup>19</sup>, H. F. van Beek<sup>20</sup>, J. Rodríguez-Pacheco<sup>21</sup>, and R. P. Lin<sup>2</sup>

<sup>1</sup> University of Applied Sciences and Arts Northwestern Switzerland, Bahnhofstrasse 6, 5210 Windisch, Switzerland

<sup>2</sup> Space Sciences Laboratory, University of California, 7 Gauss Way, 94720 Berkeley, USA  
e-mail: krucker@berkeley.edu

<sup>3</sup> ETH Zürich, Rämistrasse 101, 8092 Zürich, Switzerland

<sup>4</sup> Paul Scherrer Institute, 5232 Villigen PSI, Switzerland

<sup>5</sup> Space Research Centre, Polish Academy of Sciences, Bartycka 18A, 00-716 Warsaw, Poland

<sup>6</sup> Astronomical Institute, University of Wrocław, Wrocław, Poland

<sup>7</sup> IRFU, CEA, Université Paris-Saclay, and Université Paris Diderot, AIM, Sorbonne Paris Cité, CEA, CNRS, 91191 Gif-sur-Yvette, France

<sup>8</sup> IRFU, CEA, Université Paris-Saclay, 91191 Gif-sur-Yvette, France

<sup>9</sup> LESIA, Observatoire de Paris, Université PSL, CNRS, Sorbonne Université, Université de Paris, 5 place Jules Janssen, 92195 Meudon, France

<sup>10</sup> School of Physics and Astronomy, University of Minnesota, Minneapolis, MN 55455, USA

<sup>11</sup> Astronomical Institute, The Czech Academy of Sciences, Ondřejov, Czech Republic

<sup>12</sup> Leibniz-Institut für Astrophysik Potsdam (AIP), An der Sternwarte 16, 14482 Potsdam, Germany

<sup>13</sup> Institute of Physics, University of Graz, 8010 Graz, Austria

<sup>14</sup> Astrophysics Research Group, School of Physics, Trinity College Dublin, Dublin 2, Ireland

<sup>15</sup> School of Cosmic Physics, Dublin Institute for Advanced Studies, 31 Fitzwilliam Place, Dublin D02 XF86, Ireland

<sup>16</sup> Northumbria University, NE1 8ST Newcastle upon Tyne, UK

<sup>17</sup> Dipartimento di Matematica, Università di Genova, via Dodecaneso 35, 16146 Genova, Italy

<sup>18</sup> NASA Goddard Space Flight Center and Catholic University of America, Greenbelt, MD 20771, USA

<sup>19</sup> Solar Physics Laboratory, Code 671, NASA Goddard Space Flight Center, Greenbelt, MD, USA

<sup>20</sup> Van Beek Consultancy, Arnhem, The Netherlands

<sup>21</sup> Universidad de Alcalá, Space Research Group, 28805 Alcalá de Henares, Spain

Received 19 December 2019 / Accepted 21 January 2020

### ABSTRACT

**Aims.** The Spectrometer Telescope for Imaging X-rays (STIX) on Solar Orbiter is a hard X-ray imaging spectrometer, which covers the energy range from 4 to 150 keV. STIX observes hard X-ray bremsstrahlung emissions from solar flares and therefore provides diagnostics of the hottest ( $\gtrsim$ 10 MK) flare plasma while quantifying the location, spectrum, and energy content of flare-accelerated nonthermal electrons.

**Methods.** To accomplish this, STIX applies an indirect bigrid Fourier imaging technique using a set of tungsten grids (at pitches from 0.038 to 1 mm) in front of 32 coarsely pixelated CdTe detectors to provide information on angular scales from 7 to 180 arcsec with 1 keV energy resolution (at 6 keV). The imaging concept of STIX has intrinsically low telemetry and it is therefore well-suited to the limited resources available to the Solar Orbiter payload. To further reduce the downlinked data volume, STIX data are binned on board into 32 selectable energy bins and dynamically-adjusted time bins with a typical duration of 1 s during flares.

**Results.** Through hard X-ray diagnostics, STIX provides critical information for understanding the acceleration of electrons at the Sun and their transport into interplanetary space and for determining the magnetic connection of Solar Orbiter back to the Sun. In this way, STIX serves to link Solar Orbiter's remote and in-situ measurements.

**Key words.** instrumentation: miscellaneous – Sun: X-rays, gamma rays – Sun: chromosphere – Sun: corona

## 1. Introduction

The Spectrometer/Telescope for Imaging X-rays (STIX) supports the Solar Orbiter mission (Müller et al. 2020; Auchère et al. 2020; Walsh et al. 2020; Zouganelis et al. 2020; Rouillard et al. 2020) with hard X-ray imaging spectroscopy measurements, providing diagnostics of the hottest ( $\gtrsim 10$  MK) thermal plasmas in the solar corona and information on nonthermal electrons that are accelerated above  $\sim 10$  keV during solar flares. Hard X-ray spectroscopy in the 4 to 150 keV range at 1 keV resolution is achieved by using passively cooled Cadmium Telluride (CdTe) X-ray detectors. The instrument employs a Fourier-transform imaging technique, used by both the Hard X-ray Telescope (Kosugi et al. 1991) on the Japanese Yohkoh mission and the Hard X-ray Imager on the upcoming Chinese ASO-S mission (Zhang et al. 2019; Gan et al. 2019), and related to that used for the Reuven Ramaty High Energy Solar Spectroscopic Imager (RHESSI) mission (Lin et al. 2002). The indirect imaging concept of STIX is well-suited to the limited mass, power, and telemetry resources available for the Solar Orbiter payload. For example, each STIX image can be transmitted with as little as 100 bytes.

The next section briefly outlines the core of the STIX science objectives in view of the general Solar Orbiter science. The instrument overview is then presented in Sect. 3 followed by sections on the imaging (Sect. 4), detector and electronics (Sect. 5), and onboard data handling (Sect. 6). The STIX operation concept, data products, and analysis considerations are discussed in Sect. 7.

## 2. Science objectives

The dominant emission mechanism in the STIX hard X-ray energy range is bremsstrahlung, which is produced when energetic electrons decelerate in the solar corona as they encounter ambient protons. In general only the highest energy electrons in the solar corona have enough energy to produce bremsstrahlung above the STIX lower energy range. STIX with its energy range from 4 to 150 keV therefore provides information on the tail of the electron distribution, which gives diagnostics of the most energetic electrons. Hence, hard X-ray emissions provide ideal diagnostics of the hottest plasmas in solar flares and of the non-thermal tails seen at energies above the hottest thermal population (for reviews see Fletcher et al. 2011; Holman et al. 2011; Kontar et al. 2011).

Typical hard X-ray flare spectra are shown in Fig. 1 with the thermal distribution seen best at lower energies, while the high energies are produced by nonthermal electrons. For smaller flares which tend to be cooler, the energy above which nonthermal emission is seen is generally lower, and it can reach values below 10 keV (e.g., Hannah et al. 2008). As the bremsstrahlung emission mechanism is well understood, the observed spectra provide quantitative diagnostics on the thermal plasma and the accelerated electrons (e.g., Brown 1971).

In summary, solar flare hard X-ray observations give quantitative measurements of energy release processes in solar flares. The remote-sensing X-ray measurements made with STIX determine the intensity, spectrum, timing, and location of accelerated electrons near the Sun. Simultaneously, the size, density, temperature, and energy content of the flare-heated plasma are determined. Specifically, for well-observed flares, the spectral deconvolution of the X-ray imaging-spectroscopy observations enable both the temperature and emission measure of thermal plasmas and the number and energy spectrum of nonthermal electrons to be determined on both a spatially-integrated and

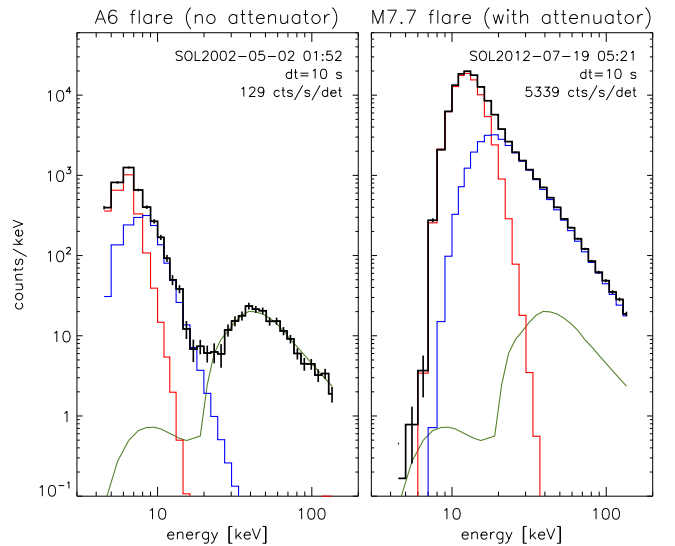


**Fig. 1.** Expected STIX HXR count spectra for two real flares (GOES A6 and M7.7), shown as 10 s accumulations in default STIX science energy channels. In each plot, the black histogram with photon counting uncertainties is the detector-summed count spectrum made up of the thermal (red), nonthermal (blue), and background (green) components. Note that the contribution of the on-board calibration sources are not included in these simulations, and the background at low energies therefore appears artificially low.

**Table 1.** STIX specification summary.

Energy range	4–150 keV
Energy resolution (FWHM)	1 keV at 6 keV
Effective area	6 cm <sup>2</sup>
Finest angular resolution	7 arcsec
Field of view for imaging	2 × 2 degree
Image placement accuracy	4 arcsec
Time resolution	0.1 to 1 s
Nominal power	~8 W
Mass (excluding window)	6.58 kg
Telemetry	700 bits s <sup>-1</sup>

feature-associated basis. By using this set of diagnostics, STIX plays an important role in enabling Solar Orbiter to achieve two of its major science goals: (1) understanding the acceleration of electrons at the Sun and their transport into interplanetary space and (2) determining the magnetic connection of the Solar Orbiter back to the Sun. Therefore, STIX provides an important link between the remote and in-situ instruments of the Solar Orbiter mission.

## 3. Instrument overview

The STIX instrument provides imaging spectroscopy of solar flare X-ray emission. Instrument performance is summarized in Table 1.

The hardware consists of three main subsystems (Fig. 2):

- A pair of X-ray transparent entrance windows, independently mounted in the heat shield of Solar Orbiter;
- An imager with two widely separated grids, independently mounted on the spacecraft (s/c) Y panel, and containing key elements of the STIX aspect system;

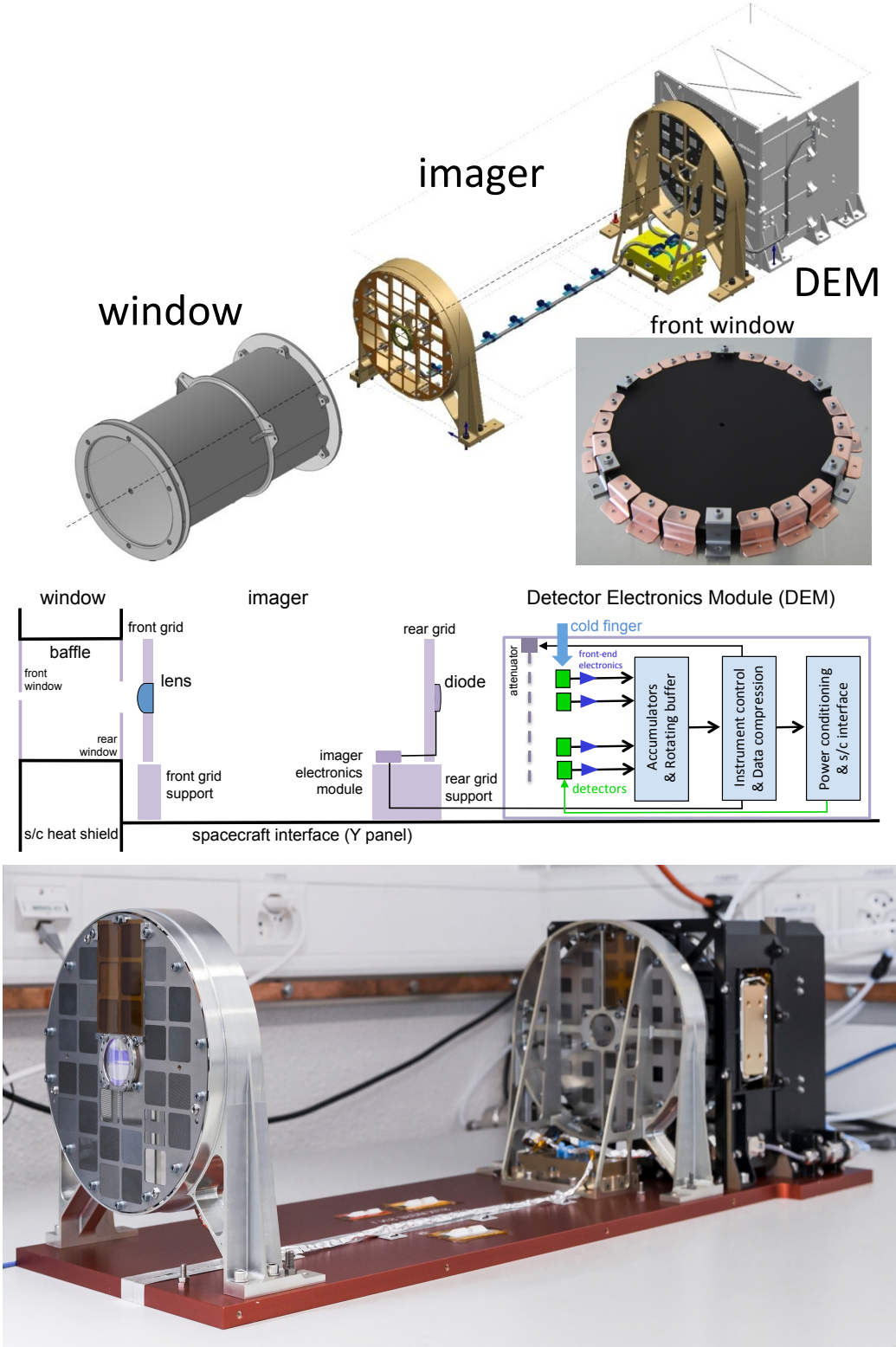


**Fig. 2.** Drawing, functional, and photographic views of the STIX instrument, as described in the text. The inset (top) shows the front window, its six decoupling springs and copper thermal straps. Note that the photo of the instrument (bottom) has been mirrored to match the orientation in the other panels.

– A Detector/Electronics Module (DEM), mounted behind the imager, containing electronics and cadmium telluride (CdTe) detectors, and a movable X-ray attenuator.

The following paragraphs introduce the individual subsystems which are then described in more detail in subsequent sections.

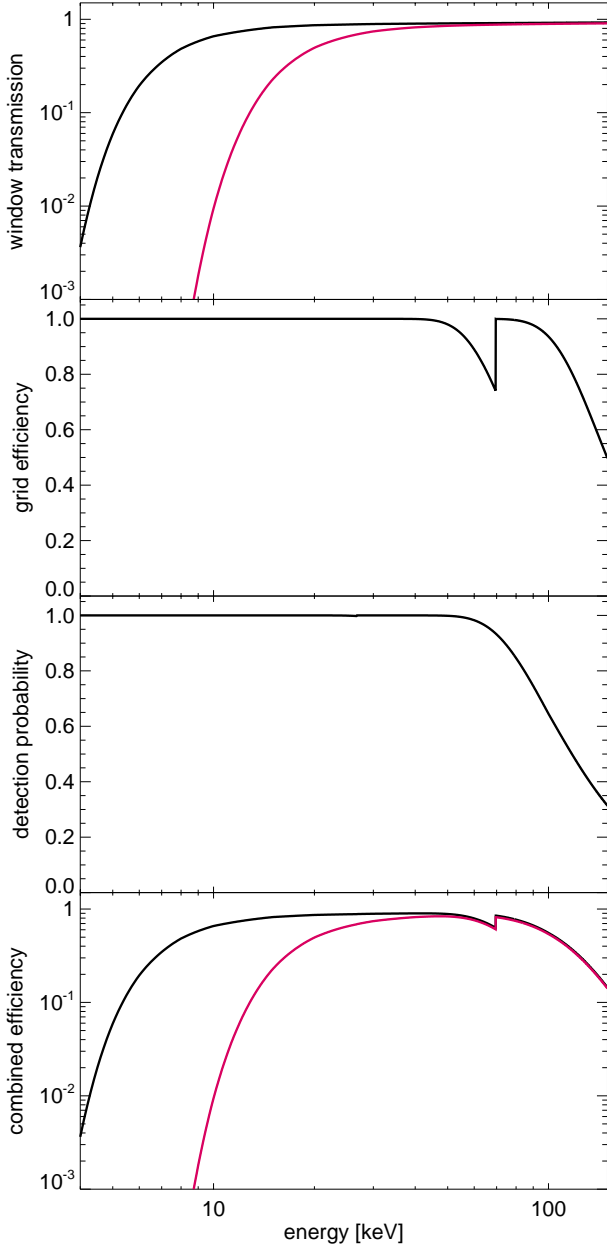


**Fig. 3.** Limiting factors for STIX energy range. The transmission through the STIX windows (front and rear combined) is shown in the top panel with (red) and without (black) the attenuator inserted. The effect of grid transparency on the measurement of visibilities is shown in the second panel as the “grid efficiency” while the probability of detection is shown in the third. Bottom panel: resulting combined imaging efficiency with and without attenuator.

### 3.1. Window

The STIX X-ray windows (Fig. 2) play two roles. First, they are prime elements in the instrument thermal control system, reflecting or re-radiating most of the incident radiation so as to limit the optical and IR solar flux seen by the instrument itself and the s/c interior. Second, they serve to preferentially absorb the intense flux of low energy X-rays that would otherwise result in excessive count rates, pulse pileup, and dead time in the detectors during intense flares. Using low-Z materials (primarily optical grade beryllium), the thermally-effective window has X-ray absorption properties that permit observations down to 4 keV (Fig. 3). In

terms of mounting, the 2 mm thick front window is attached via 6 decoupled springs to a feedthrough provided by Solar Orbiter. The 1 mm thick rear window is directly attached to the rear of the heatshield feedthrough (Fig. 2). To increase the margin on the thermal design, the front window is coated with Solar Black, the same coating used for the Solar Orbiter heatshield. The front and rear windows have 5 and 25 mm diameter open apertures, respectively, for use by the aspect system.

### 3.2. Imager

High-resolution solar hard X-ray imaging within the mass and volume constraints of Solar Orbiter currently precludes the use of focusing optics (e.g., Krucker et al. 2014). Instead it requires non-focusing, grid or mask-based techniques (e.g., Hurford 2013). STIX uses Fourier-transform bigrid imaging to achieve the high angular resolution required for solar sources, an approach that is also well-suited to a limited-telemetry environment.

The imager hardware consists of two X-ray opaque grids separated by 55 cm that are independently mounted on the s/c Y panel (Fig. 2). Each of these grids is divided into 32 subareas with a corresponding set of 32 coarsely-pixelized detectors located behind the rear grid. A pair of corresponding subareas and its detector is termed a “subcollimator” (see Figs. 4 and 5).

Within each subcollimator, the grids contain a large number of parallel, equispaced slits. The slits in the corresponding front and rear grids windows differ slightly in pitch and/or orientation. These differences are selected so that, for each window, the combined X-ray transmission of the grid pair forms a large-scale Moire pattern on the detector (see Fig. 4, right) with a period equal to the detector width and oriented to be parallel to a detector edge (see Sect. 4.2). The amplitude and phase of this pattern are very sensitive to the angular distribution of the incident X-ray flux (Fig. 6). Thus the high-angular resolution X-ray imaging information is encoded into a set of large-scale spatial distributions of counts in the detectors.

The grid design provides the imaging information in the form of a set of angular Fourier components of the source distribution (visibilities) in analogy with the imaging information provided by antenna pairs in a radio interferometer. The set of measured visibilities is then used on the ground to reconstruct an image of the X-ray source (Sect. 4.3).

Elements of the STIX aspect system are embedded in the center of the front and rear grids as discussed in Sect. 4.6.

### 3.3. Detector electronics module (DEM)

The DEM is in the form of a single module that contains almost all the active instrument electronics. Specifically, its content and purpose include:

- 32 coarsely pixelized CdTe detectors;
- A set of 128 weak  $^{133}\text{Ba}$  radioactive sources that illuminate the detectors with X-ray. The two strongest lines of the  $^{133}\text{Ba}$  spectrum at 31 and 81 keV are used for energy calibration;
- Front-end electronics that handle initial amplification, pulse shaping and processing of the detector output;
- An internal enclosure (Cold Unit) that thermally isolates the detectors and front-end electronics. This enables passive cooling to maintain them at temperatures well below  $-15^\circ\text{C}$ ;
- A movable aluminum attenuator that can be inserted during high-rate periods to further limit the detectors’ exposure to high fluxes of low energy flare X-rays;

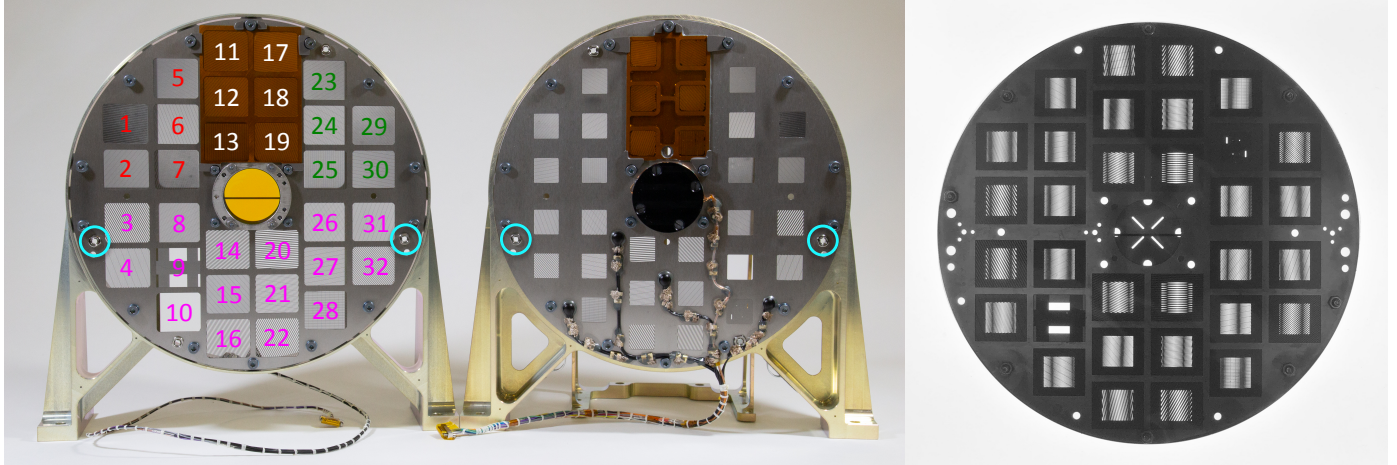


**Fig. 4.** Photo of STIX flight-spares front (*left*) and rear (*center*) grids, mounted in their grid support frames. The front grid assembly is seen from the Sun side, while the rear grid is seen from the detector side (so that for window comparisons, one should mentally “flip” the rear grid). The numbers indicate subcollimator labels (similar colors correspond to grids that were etched on the same foils). The blue circles indicate the locations of fiducials, used for optical characterization and grid-to-grid alignment. Individual windows are  $22 \times 20$  mm (front) and  $13 \times 13$  mm (rear). On the right, a back-illuminated picture of a front grid on top of a rear grid is shown to highlight the created Moire patterns. This Moire picture uses an early prototype grid with different assignment of the individual windows.

- Analog to digital converters for the X-ray detectors’ output;
- An Instrument Data Processing Unit (IDPU) which performs all digital processing of the X-ray data;
- Low-voltage and high-voltage power supplies;
- Interfaces to spacecraft power and SpaceWire signals.

Power supplies and digital electronics are duplicated and cross-strapped to provide cold redundancy. The aspect system electronics are housed in a small “Instrument Electronics Module” (IEM) module attached to the rear grid mount. Details on the functions and implementation of the DEM are given in Sects. 5 and 6.

## 4. Imaging

In this section, we describe the imaging concept and its implementation on STIX.

As previously mentioned, the STIX imager consists of two X-ray opaque grids, separated by 55 cm (Fig. 2). As shown in Fig. 4, each grid is divided into 32 subareas. Thirty of these “windows” each contain large numbers of equispaced, parallel slats and slits (Fig. 5). (The remaining two grid windows serve special purposes, described in Sects. 4.4 and 4.5). The front and rear windows are  $22 \times 20$  mm and  $13 \times 13$  mm, respectively. An X-ray detector with coarse spatial resolution is located behind each pair of windows (Fig. 2).

### 4.1. Grids

Within each subcollimator, there is a small but deliberate difference in the pitch and/or orientation of the slits in the front and rear grids. For parallel incident X-rays, this results in the combined transmission of the grid pair forming a large-scale Moire pattern on the face of the corresponding detector (Sect. 4.2). The amplitude and phase of this spatial Moire pattern provides a direct measurement of a Fourier component (visibility) of the angular distribution of the source. In practice, the measurement is of the Cartesian representation of the visibility (real and imaginary components), which is interchangeable with the polar representation of amplitude and phase.

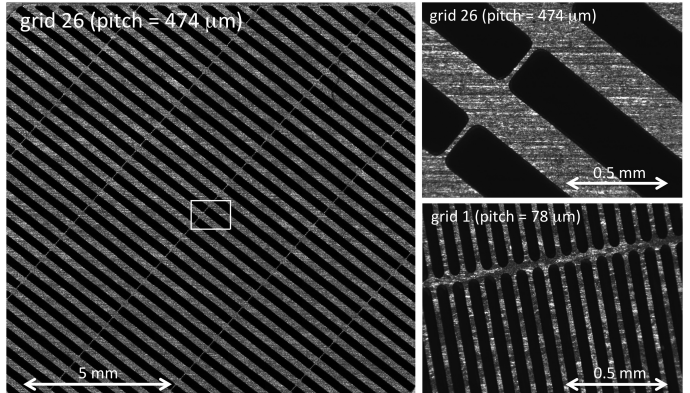


**Fig. 5.** Closeup of one of the rear grids (number 26) seen with front illumination is shown on the *left*. The slats run from lower right to upper left. The five faint orthogonal lines from the lower left to the upper right are “bridges” which add structural strength but do not degrade imaging. The image on the *top right* shows a closeup of the same grid, corresponding to the white box on the left. *Bottom right*: closeup of a much finer pitch grid (number 1).

The grids were fabricated by Mikro Systems Inc (Charlottesville, VA) using a technique similar to that used for the fine RHESSI grids (Lin et al. 2002). Specifically, 4 to 12 layers of 35 to  $100\text{ }\mu\text{m}$  thick tungsten foils were etched and then stacked to create a grid that is effectively  $400\text{ }\mu\text{m}$  thick<sup>1</sup>.

<sup>1</sup> Special provisions were made in the fabrication of the six grids with the finest pitches, 54 and  $38\text{ }\mu\text{m}$ , (marked with white numbers in Fig. 4), to deal with the difficulty in etching  $22$  and  $30\text{ }\mu\text{m}$  wide slits in relatively “thick” material. For the  $54\text{ }\mu\text{m}$  pitch case, the individual layers were divided into two “phased” subsets with every even slat omitted in one subset and every odd slat omitted in the other. Both subsets were then stacked together to form a grid with the correct effective pitch of  $54\text{ }\mu\text{m}$  but with only half the X-ray effective thickness. A similar technique was used for the finest grids with  $38\text{ }\mu\text{m}$  pitch, except that the layers were etched as three “phased” subsets prior to being stacked. Since the slats in these grids were relatively narrow, the subareas were encased in an additional thin layer of Kapton (see Fig. 2).

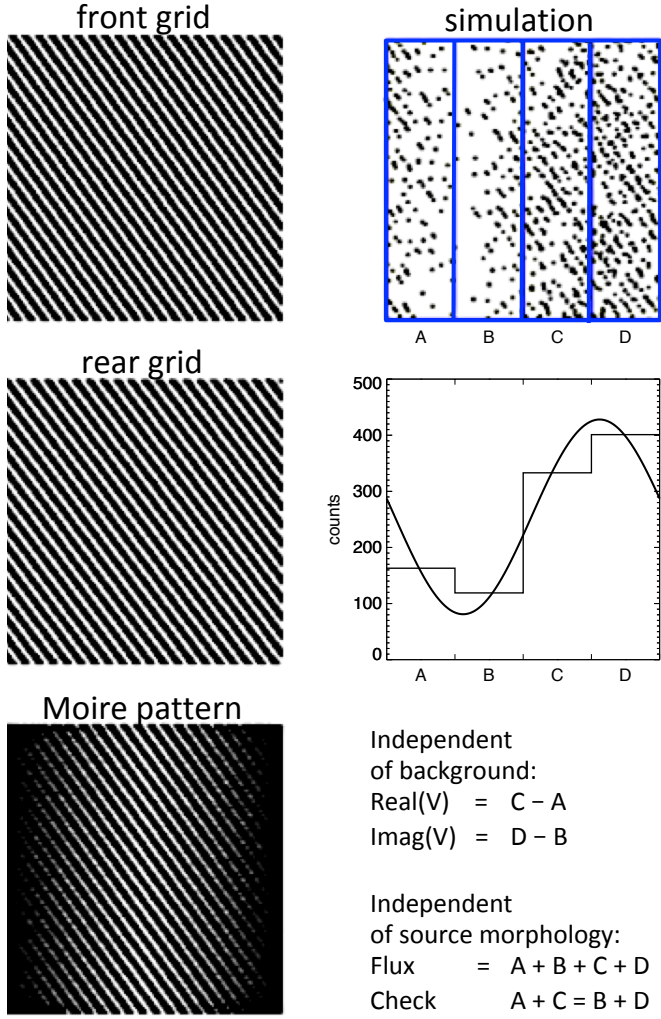


**Fig. 6.** Measurement of a visibility. Two panels on the top-left: front/rear pair of grids for one subcollimator. Close inspection shows that they have slightly different pitch and orientation. The combined transmission for an on-axis point source yields a Moire pattern (bottom-left panel). A simulation for an off-axis source shows the location of detected photons (top-right panel), as seen by a detector with four large pixels (blue). Accumulated counts in the four pixels are shown in the center-right panel. Differences among these counts (bottom right) yield the real and imaginary components of the Fourier component independent of background. The sum over the four pixels yields the flux (+background), independent of the visibility. There is also a cross check that is independent of the visibility, flux, and background.

As-built parameters of the grids were confirmed by 2-D optical scanning with  $\sim 2 \mu\text{m}$  resolution and with  $\sim 15 \text{ keV}$  X-rays using the Swiss Light Source at the Paul Scherrer Institute. The optical measurements were used to determine the grid pitch, orientation and phase, while X-ray imaging provided a more robust measurement of slit width.

#### 4.2. Visibilities

The data from each subcollimator can be interpreted as a measurement of a specific Fourier component of the source angular distribution. The specific Fourier frequency of this measurement depends on the average orientation and pitch of the slits and on the grid separation. The Fourier period is given by the ratio of the average pitch to the grid separation (the angular resolution of

a subcollimator is defined as half the period<sup>2</sup>). The finest grid pitch used on STIX is  $38 \mu\text{m}$  which provides an angular resolution of  $(1/2 \times 38 \text{ microns}/550 \text{ mm}) = 0.0345 \text{ milliradians}$  or  $7.1 \text{ arcsec}$ . In terms of orientation, the sensitivity is perpendicular to the slits. It is worth noting that with this type of imager, the complete X-ray angular response can be inferred from a set of two-dimensional measurements of the individual grids. Direct measurement of the point-response-function of the integrated telescope is not needed.

The period and orientation of the Moire pattern is determined by the vector difference of spatial frequencies of the chosen front and rear grids. For each subcollimator the difference was chosen to yield a Moire pattern with a period equal to the active width of each detector (8.8 mm) and with the orientation of the Moire fringes parallel to the long axis of the detector pixels (viz. parallel to the s/c Y axis). Thus, each detector sees one complete Moire period over its active area (Fig. 6).

Note that the orientation and period of the Moire pattern is a design parameter and so contains no X-ray imaging information itself. It does, however, directly measure any unexpected grid-to-grid or grid-to-detector misalignment whose effects can then be mitigated during analysis.

The nominal imaging properties of the set of subcollimators are determined by the distribution of the chosen angular Fourier components. STIX measures 10 different angular resolutions, logarithmically spaced between  $7.1$  and  $179 \text{ arcsec}$  in steps of 1.43. Logarithmic spacing was chosen to provide sensitivity to a wide range of source angular sizes. The finest spatial frequency corresponds to an angular resolution of  $7.1 \text{ arcsec}$ . Measurements at intermediate angular frequencies provide the information needed to measure source size and shape at intermediate scales. At each angular frequency, there are three subcollimators with different orientations. The measured angular frequencies (uv coverage) are plotted in Fig. 7 along with examples of corresponding point response functions when these visibilities are combined. Angular frequencies and grid parameters for each of the 30 Fourier subcollimators are given in Table 2.

For a single simple source, a visibility amplitude is proportional to its total flux, but also depends on the size and shape of the source. For a simple source, the ratio of visibility amplitude to total flux can provide a measure of its size. The visibility phase depends on the source location and/or its morphology. The choice of the coarsest spatial frequency determines the maximum diffuse source size that can be imaged ( $\sim 180 \text{ arcsec}$ ). Widely separated compact sources, however, can be effectively imaged regardless of their separation.

The measured visibilities themselves have several useful properties. For example, visibilities are linear in two senses. Visibility amplitudes scale linearly with the incoming flux, so that visibilities corresponding to different energies and/or times can be linearly combined without introducing systematic errors. Thus, by acquiring data in relatively narrow energy and/or time bins, the analyst retains the option of combining these to enhance statistics over broader time and/or energy bins. Viewing linearity from a second perspective, the visibility of a multi-component source is just the (complex) sum of the visibilities of its components. This property is useful for interpreting and/or anticipating the visibility of more complicated source morphologies.

<sup>2</sup> The FWHM of the point response function of the synthesized beam that is formed by combining multiple visibilities depends on the relative weighting of the visibilities. This is generally broader than the resolution of the finest subcollimator. Note, however, that the location of a source can be determined to much better accuracy than this resolution.

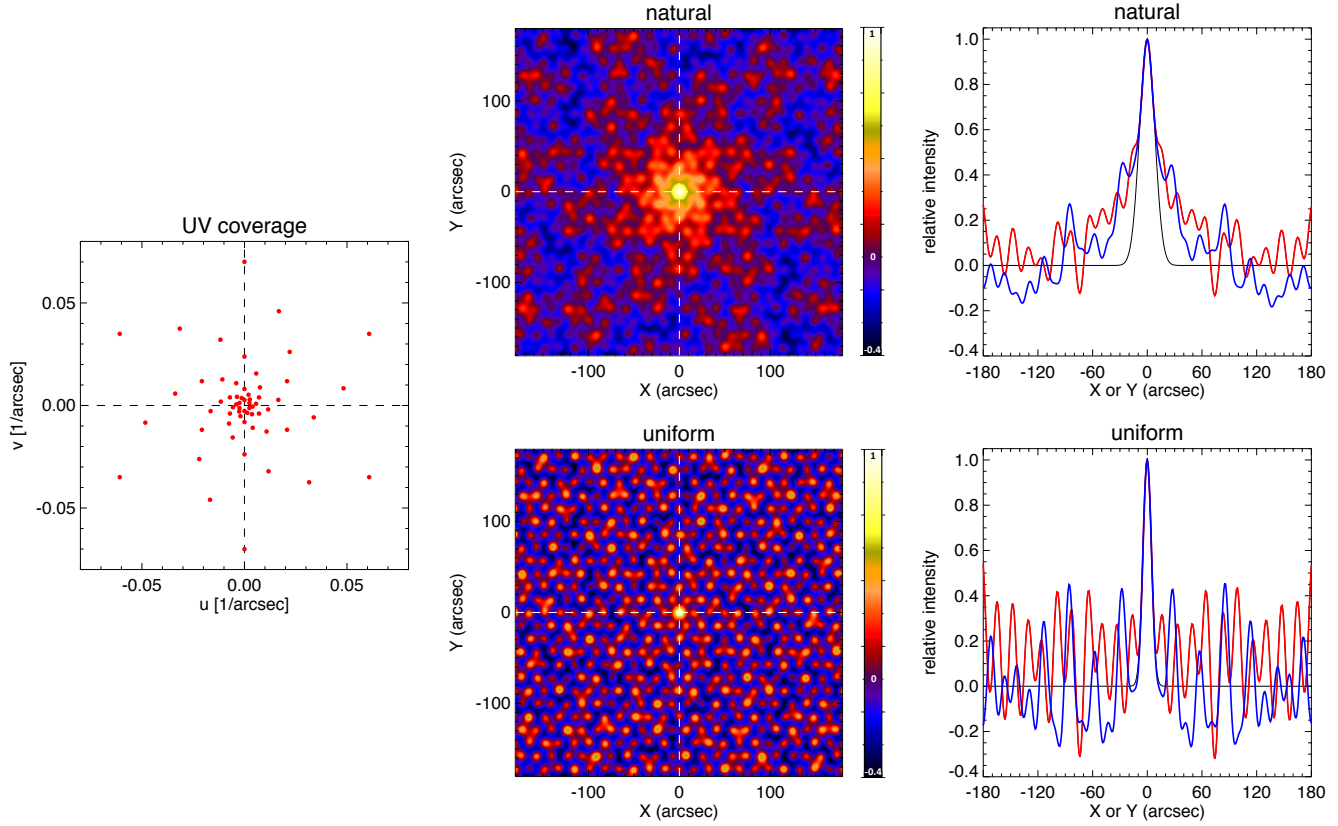


**Fig. 7.** Left: angular frequency ( $uv$ ) coverage provided by the 30 STIX Fourier components. The corresponding point response function, is shown over a  $360 \times 360$  arcsec FOV (top center) and as profiles along the  $x$  and  $y$  axes (top right) with equal (natural) weighting of all 30 visibilities which yields a FWHM beam of  $\sim 19$  arcsec (black profile). Alternative weighting choices provide the post-facto ability to trade imaging dynamic range for higher angular resolution in the point response function. For “uniform” weighting (proportional to spatial frequency), the FWHM becomes 11 arcsec (bottom center and right). The imaging FOV can be selected post-facto anywhere on the Sun.

**Table 2.** Nominal grid parameters.

Grid label	Subcollimator number	Average pitch [mm]	Slit width [mm]	Average orientation [degrees]	Angular resolution [arcsec]
1 a,b,c	11,13,18	0.0380	0.0220	150,90,30	7.1
2 a,b,c	12,19,17	0.0543	0.0302	130,70,10	10.2
3 a,b,c	7,29,1	0.0777	0.0419	110,50,170	14.6
4 a,b,c	25,5,23	0.1112	0.0586	90,30,150	20.9
5 a,b,c	6,30,2	0.1590	0.0825	70,10,130	29.8
6 a,b,c	15,27,31	0.2275	0.1168	50,170,110	42.7
7 a,b,c	24,8,28	0.3254	0.1657	30,150,90	61.0
8 a,b,c	21,26,4	0.4655	0.2358	10,130,70	87.3
9 a,b,c	16,14,32	0.6659	0.3360	170,110,50	124.9
10 a,b,c	3,20, 22	0.9526	0.4793	150,90,30	178.6
CFL	9				
BKG	10				

Another useful property of visibilities follows from the fact that they are measured as linear combinations of count rates in different pixels (Fig. 6). Therefore Poisson statistics in the original accumulated data can be directly converted to statistical errors in the resulting visibilities. Depending on the choice of image reconstruction algorithm, such visibility errors can then be directly interpreted in terms of statistical errors in the source properties themselves.

#### 4.3. Image reconstruction

The relationship between an image,  $I(x, y)$  and its visibilities,  $V(u, v)$ , is well-known, with each visibility given as:

$$V(u, v) = \int \int I(x, y) e^{i(ux+vy)} dx dy \quad (1)$$

where the integration is over the full angular field of view and  $(u, v)$  are the Cartesian components of the measured angular frequency.

With measurements of visibilities at many values of  $(u, v)$ , the image can be formally reconstructed by the inverse Fourier transform:

$$I(x, y) = \int \int V(uv) e^{-i(ux+vy)} du dv. \quad (2)$$

Image reconstruction from a discrete set of measured visibilities is based on adaptations of well-developed techniques widely used in radio interferometry, where the direct observables are also a set of visibilities of the source angular distribution (obtained in this case from the correlated signals from separated antennas). Reconstruction techniques include back projection, which represents the convolution of the source and the point-spread-function, corresponding to a “dirty map” in radio interferometry; Clean, which removes the sidelobe responses for multiple point sources; maximum entropy; count-based imaging methods (e.g., Massa et al. 2019); Bayesian techniques; etc.

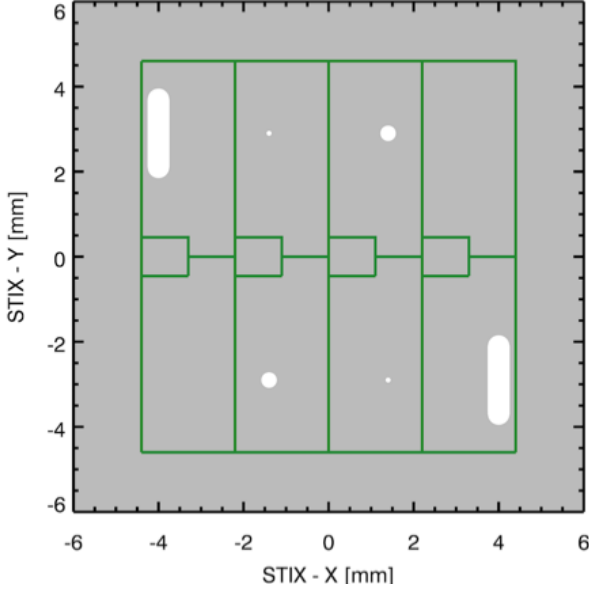


**Fig. 8.** Pattern of 6 small apertures (white) on the otherwise solid rear BKG grid (gray), projected onto the detector pixels (green) for an on-axis source.

The primary difference<sup>3</sup> is that in X-ray imaging, relatively few visibilities are available (30 in this case) compared to the hundreds to many thousands typically available in radio. This limits the complexity of the X-ray source that can be effectively imaged. One measure of image quality, also used in radio, is the dynamic range, which is the ratio of the intensity of the strongest to the weakest believable source in the reconstructed image. For STIX the design and calibration goal is that for a strong isolated source, a dynamic range of 20:1 can be achieved<sup>4</sup>.

#### 4.4. Background measurement

Two of the 32 subcollimators are not used to measure Fourier components. One of these, the “BKG” subcollimator, monitors both the X-ray background and the intense unattenuated low-energy flux from large flares. The BKG subcollimator is never covered by the attenuator and combines an open front grid window with a rear grid window that is fully opaque except for six small apertures (two each of 0.01, 0.1, and 1 mm<sup>2</sup>, see Fig. 8). As needed during large flares, successive pixels in this detector can be automatically disabled. Thus the small, graduated sizes of the apertures enable the remaining active pixels to monitor both background and incident flux while avoiding excessive count rates.

#### 4.5. Coarse flare location

The role of the 32nd subcollimator is to provide a real-time coarse, but unambiguous, flare location relative to the STIX optical axis. For this “CFL” subcollimator, the rear grid window is open and the front grid window has a coarse “H-shaped” pattern (Fig. 9). Its geometry and dimensions are chosen to enable each potential flare location to provide the CFL detector with a unique

<sup>3</sup> An additional difference is that radio uses Gaussian statistics, while X-ray analyses often use Poisson statistics. However for X-ray imaging, counts are summed over sufficiently broad time and/or energy ranges that the former can be used.

<sup>4</sup> In practice, two other factors, limited photon statistics and the source morphology, reduce the dynamic range below this value.

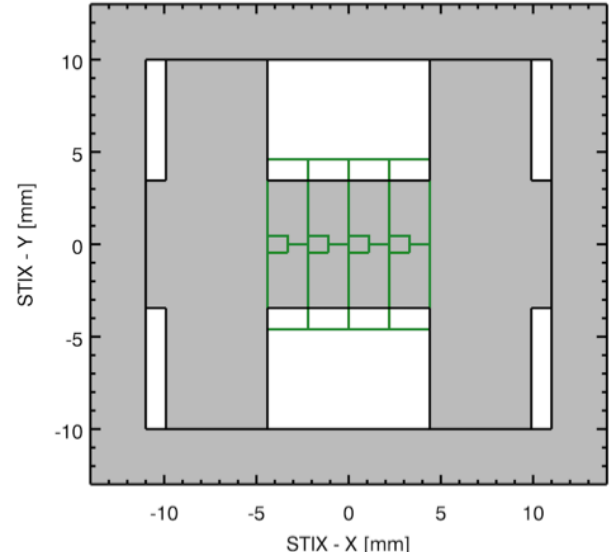


**Fig. 9.** Pattern of large apertures on the front grid for the CFL subcollimator. Its X-ray shadow (gray) is shown superimposed on the detector pixels (green) for an on-axis source. Different source locations can be visualized by shifting the detector relative to the mask.

pattern of pixel illumination over a 2×2 degree field of view. The onboard processing for the CFL is discussed in Sect. 6.3.2.

#### 4.6. Aspect

Aspect knowledge is required to compensate for potentially unstable pointing and to correctly place the reconstructed X-ray image on the Sun for comparison with other images.

STIX uses the spacecraft aspect solution for roll and relative pitch-yaw aspect. This ensures the integrity of the image morphology since changes in s/c pointing during an image integration time can be fully compensated post-facto by noise-free adjustments to the visibility phases.

However, the spacecraft aspect cannot support accurate determination of the absolute position of the X-ray source on the Sun. This is because on longer (multi-week) timescales, thermo-elastic deformation of the spacecraft and/or STIX mechanical structures can change the relative direction of the STIX optical axis and the s/c reference axis. These changes must be mitigated since they are expected to exceed the goal of 4 arcsec for the uncertainty in STIX absolute source positions.

To establish the relationship between the s/c reference axis and the STIX imaging axis, the STIX aspect system (Fig. 10; for details see Warmuth et al. 2020) uses a 28 mm (effective) diameter plano-convex lens in the front grid assembly to focus a 550–700 nm optical image of the Sun onto the rear grid<sup>5</sup>. Measurement of the position of the solar optical limbs on the rear grid plane then locates the STIX imaging axis with respect to the direction to Sun center. The key design feature is that the position of the critical aspect system elements (lens and solar image detector) are fixed within the grids themselves. Thus the locations of the lens center and solar image are accurately known relative to the X-ray slits. This enables the aspect calibration to be independent of the mechanical properties of the grid mounts and the s/c-dependent mechanical linkage between the front and rear grids.

<sup>5</sup> This lens is illuminated through an open 5 mm diameter aperture in the center of the front X-ray window. The precise aperture location does not influence the aspect calibration.

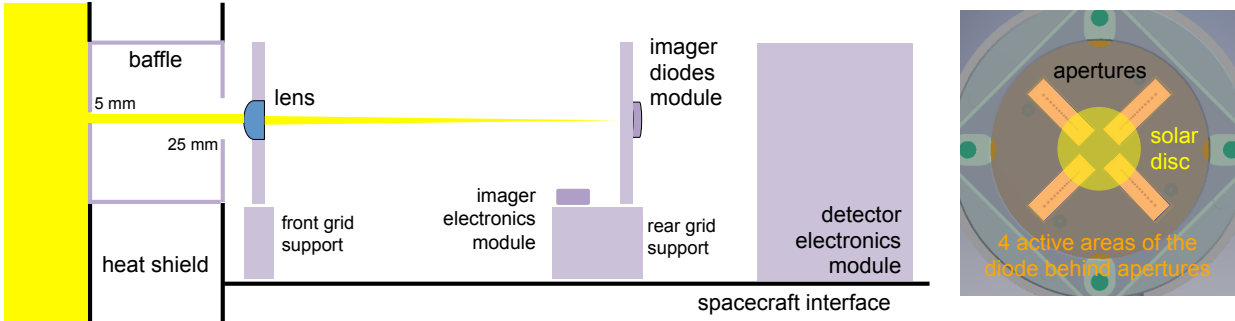


**Fig. 10.** Schematic view of the STIX aspect system. Viewing the Sun through a 5 mm diameter opening in the front window, a lens in the front grid focuses an image of the solar disk onto four rows of small apertures in the rear grid. Four large photodiodes integrate the light passing through a corresponding row of apertures. When a solar limb passes over one of the apertures, the output of that diode changes by ~20%. Such transitions provide an occasional but accurate measurement of the location of the solar image relative to the rear grid slits.

Instead of using linear diode arrays to measure the location of the solar limbs on the rear grid, a simpler system is used which provides only the required occasional measurement of the limb location. Small (90 to 300 micron) circular apertures are etched into the rear grid, in the form of four orthogonal radial rows in the center of the rear grid assembly (Fig. 10, right panel). Behind these apertures, four photodiodes<sup>6</sup> record the integrated light passed by each row of apertures. When the solar limb passes over one of these apertures, there is a step-wise change in the output of the corresponding photodiode. Post-facto comparisons of the spacecraft aspect solution at such times establishes the offset between the STIX imaging axis (as defined by the lens center and aperture pattern) and the spacecraft aspect. Since orbital motion continually changes the apparent solar diameter, such crossings occur every few days even if the s/c pointing is stable.

The s/c aspect solution is also used for relative roll aspect. The application to STIX can be calibrated by imaging a cosmic X-ray source (such as the Crab) when it passes within 1 degree of the Sun. The orientation of the locus of successive X-ray images of the cosmic source defines the absolute roll of the STIX images.

## 5. Spectrometer and data processing unit

Expanding on the introduction in Sect. 3.3, the following subsections describe the DEM components, starting with the enclosure and attenuator, followed by the detectors and front-end electronics, and lastly the Instrument Data Processing Unit (IDPU) which interfaces to the spacecraft.

### 5.1. Enclosure

The Detector/Electronics Module (DEM) was fabricated as two separate boxes:

- A Detector Box facing the Imager that encloses the movable attenuator and a cold-unit that contains the detectors and front-end electronics;
- An Instrument Data Processing Unit (IDPU) Box behind, that contains the digital electronics and power supplies.

Joined together, they form a mechanically integrated unit that bolts directly to the s/c +Y panel.

The Detector and IDPU boxes were fabricated from aluminum blocks as separate housings. After integrating and testing their respective contents, they were combined into a single structure. Mechanically, the DEM is responsible for stable posi-

tioning of the attenuator and detectors relative to the imager; thermally, it provides the path for conductive heat transport to the spacecraft mounting panel and for supporting the thermal requirements of the Cold Unit inside the Detector Box.

Interconnects between the two boxes use Omnetics connectors, mounted either directly on a printed circuit board (IDPU) or on flexible Kapton extensions (Detector Box). In addition, one external cable from the IDPU Box connects to the Imager Electronics Module (IEM) to support the aspect detectors and imager temperature sensors.

The Detector Box is shown in more detail in Fig. 11. On the front (imager side) the Detector Box is sealed with an aluminized Kapton entrance window. Since the detectors are sensitive to humidity, the DEM has provision for a purging system to allow on-ground flushing with dry nitrogen to keep the relative humidity below 5%.

### 5.2. Mechanical attenuator

After passing through the DEM entrance window, incident X-rays may next encounter the mechanical attenuator. When inserted, the attenuator preferentially reduces the flux of low-energy X-rays (compared to high-energy X-rays) to control the total count rate with minimum sacrifice of high energy counts. Its 0.6 mm thick aluminum blades are inserted and removed autonomously into the detector field of view within two seconds, based on the decision of an onboard Rate Control Regime algorithm (see Sect. 6.5). When inserted, the blades attenuate the flux at 6 keV to  $10^{-8}$ , 10 keV to 2%, and 20 keV to 60% (see Fig. 3). Attenuator operation can be disabled by telecommand.

The attenuator blades are connected to two lever arms (Fig. 11) that are acted upon by two brushless Maxon motors. One motor is nominally enough to drive the mechanism, but both can operate together as a contingency. A counterweight balances the mechanism between two pivot points. Motor power is needed only to change position. To minimize the electrical energy requirement, a power profile is used which increases linearly up to a first plateau, and then increases further to a second plateau. Power is switched off if either the end-switch signals a successful motion, or if two seconds have elapsed since the start of the profile. The level of the two plateaus can be modified by telecommand.

### 5.3. X-ray detection

The combination of the desired energy range, required high spectral resolution and low electric power budget led to the adoption

<sup>6</sup> In practice the four photodiodes are implemented as a single photodiode with four large pixels (orange rectangles in the right panel).

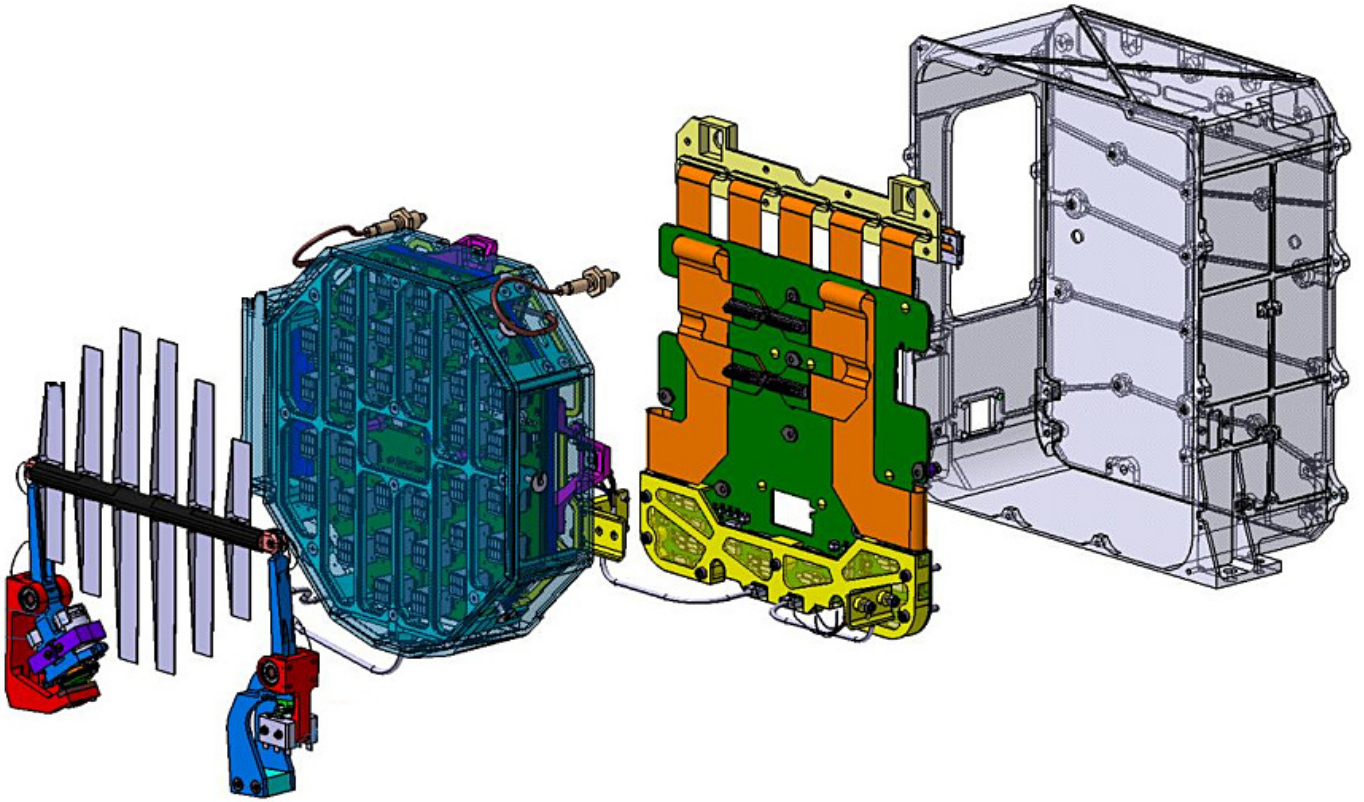


**Fig. 11.** Design of the Detector Box (*left to right*): the mechanical attenuator, the cold unit containing 32 Caliste-SO hybrids, the back-end electronics board with flex cable connections, and the housing. Not shown is the DEM entrance window to the left of the attenuator.

of passively cooled CdTe semiconductor detectors. The STIX detector system uses an array of 32 such sensors, each 1 mm thick and  $10 \times 10 \text{ mm}^2$  in area.

### 5.3.1. Properties of cadmium telluride

Since CdTe has a density of  $5.85 \text{ g cm}^{-3}$  and an average atomic number of 50, it is well suited for detection of higher energy X-rays. A 1 mm thick crystal has about 65% absorption probability at 100 keV and still about 30% at 150 keV (Fig. 3)<sup>7</sup>. The energy to create a charge carrier pair is 4.43 eV, yielding 870 pairs for a 4 keV photon. This underlines the requirement for a low-noise readout to obtain the target energy resolution of 1 keV FWHM. Low noise can only be obtained with low leakage current.

Carrier lifetimes are relatively short, typically  $\sim 3 \mu\text{s}$  for electrons and  $\sim 2 \mu\text{s}$  for holes in good quality CdTe that has few defects. It is thus important to collect the charges swiftly, which requires applying the largest possible electric field. To maintain a sufficiently low leakage current despite the high voltage, the anode of the CdTe has a Schottky electrode configuration, and the sensor temperature is kept below  $-15^\circ\text{C}$  by passive cooling through a spacecraft-provided radiator. Reverse bias in the range 200 V to 500 V is applied, much higher than would be needed for full depletion alone.

<sup>7</sup> When an incident photon interacts in a detector, it may have all or only part of its energy detected. This behavior depends on the material, its geometry, and photon energy. It is expressed in terms of a "response matrix" of detected vs photon energy, where the cases of full or partial detection represent "diagonal" or "off-diagonal" elements respectively. For the analysis of steep solar spectra, it is often (but not always) possible to use only the diagonal elements.

With such electric fields, the mean carrier drift length is many centimeters for electrons, but still only in the millimeter range for holes. For 1 mm thickness the electrons are therefore collected very nearly completely, but for holes the collection efficiency depends on the interaction depth. Above X-ray energies of about 50 keV, where interaction locations are distributed throughout the crystal, spectral lines consequently show a pronounced low-energy tail, as seen in Sect. 5.4.

### 5.3.2. Fabrication of CdTe

Raw CdTe crystals of size  $14 \times 14 \times 1 \text{ mm}^3$  with planar electrodes were procured from Acrorad (Japan) with a platinum cathode and gold-titanium-aluminum Schottky multi-layer anode. Patterning was done at the Paul Scherrer Institute using photolithography and a plasma etching process (Grimm et al. 2015). The final step was dicing to the required size of  $10 \times 10 \text{ mm}^2$ .

The pixel pattern (Fig. 12) uses four stripes to sample the Moire pattern (Fig. 6). Each stripe is sub-divided into 2 large pixels of  $9.6 \text{ mm}^2$  plus a small  $1.0 \text{ mm}^2$  pixel to help address pileup and the large dynamic range in expected count rates. Individual pixels can be disabled to reduce the trigger rate and dead time. This is done autonomously under the control of the Rate Control Regime algorithm (Sect. 6.5). A guard ring around the crystal border protects the pixels from edge-related leakage current.

Selection of flight detectors was based on the following considerations:

- Manufacturer's measurements of leakage current versus bias voltage at room temperature
- Microscopic inspections before and after the patterning process

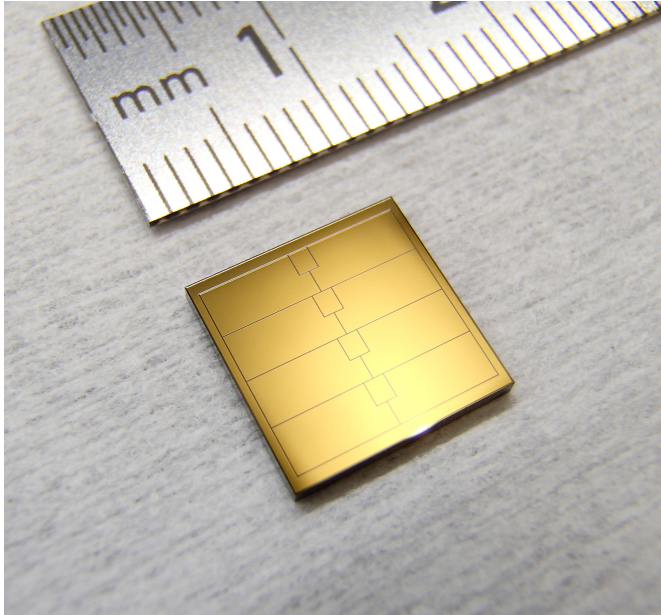


**Fig. 12.** View of the normally-hidden pixelized Schottky anode side of a STIX CdTe detector.

- Pixel-by-pixel leakage current at +20°C and –20°C
- Spectroscopic performance at –20°C as measured using  $^{133}\text{Ba}$  sources.

To obtain energy resolution below 1 keV FWHM at –20°C, the leakage current should be below 60 pA on a large pixel at 300 V bias voltage. About 80% of all processed CdTe crystal met this criteria. Unacceptable surface defects lowered this yield by a further 10%.

### 5.3.3. Caliste-SO hybrids

Each CdTe crystal was bonded to a hybrid circuit, Caliste-SO (Meuris et al. 2012), that contained the low-noise, low-power ASIC (IDeF-X HD described in Michalowska et al. (2010), plus voltage filtering and bias routing (Fig. 13). Thirteen input channels of the ASIC are routed to pads on top of the package, interfacing with the 12 pixels and the guard ring of the CdTe crystal. (The guard ring is set to the same electrical potential as the pixels for optimum protection against edge-related leakage current.) The remaining 19 available channels of the ASIC are unused and powered off in the nominal mode.

The trigger threshold can be adjusted individually for each channel. The signal shaping time can be adjusted for all channels combined, thus allowing a trade-off between rate capability (short shaping time) and lowest noise (intermediate shaping time). A value of about 5  $\mu\text{s}$  provides the lowest noise for STIX. The noise is also affected by the capacity of the pixels, resulting in better energy resolution for the small pixels (Fig. 15).

### 5.3.4. Front-end electronics

The Caliste-SO are accurately positioned and mounted on front-end electronics boards. To minimize power dissipation near the crystals, these boards contain only minimum support circuitry, high-voltage, voltage filtering, and distribution components. Other components such as the ADCs, regulators, and test pulse circuits, are mounted on a back-end board outside of the cold unit (Fig. 11). Kapton cables with low heat conductivity are used for interconnection between front-end and back-end. To

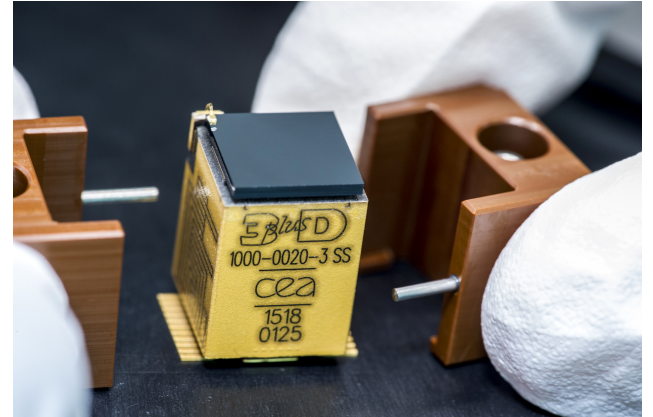


**Fig. 13.** View of Caliste-SO with a crystal mounted on the top. The picture is taken during the process of removal of the protective holder used for performance tests and transportation. The Caliste-SO body dimensions are about 11 × 12 × 15 mm high. Credit: L. Godart/CEA.

further minimize thermal leakage through control cables, each ADC services two detectors. The detector pairs are chosen so that the loss of a single ADC results in a minimum impact on imaging.

For redundancy, the front-end is electrically divided into four identical quarters. Two high-voltage channels are used, each supplying two quarters. As with the grid pairs, the relation between quarters and grid parameters was chosen to minimize the impact of the loss of any single quarter or of a single HV supply.

The total processing time for a trigger is about 12.5  $\mu\text{s}$ . This time is the same even if more than one pixel (in a detector pair) is triggered. Since the interpretation of such multiple-hit events can be ambiguous, they are subsequently discarded. A single readout is still performed, however, to guarantee that the contribution to the dead time remains the same.

### 5.3.5. Cold unit

The cold unit (see Fig. 14) is a thermally isolated enclosure within which are the detectors, Caliste, and other front-end electronics. Passive cooling is used to maintain the interior temperature and is accomplished via a STIX-dedicated radiator thermally connected to the aluminum-beryllium alloy cold plate inside the cold unit. A temperature of –25°C can be maintained at the interface to the spacecraft, provided the heat load does not exceed 3.2 W.

The inside of the spacecraft and the DEM housing will be warm during observation times near perihelion (the worst-case design temperature is +50°C), therefore the cold unit requires excellent thermal insulation. The circuit board with the Caliste-SO hybrids is mounted on the cold plate, which is insulated by Vetronite elements and multi-layer insulation (MLI). The cold unit meets the 3.2 W heat load requirement with a single-piece MLI design that combines 1.2 W to be generated electrically by the front-end electronics, plus leakage of 1 W each for conduction and radiation.

The cold unit design must also ensure that the X-ray transmission through the MLI is uniform across the front face. Otherwise false visibility signatures would be apparent in the spatial distribution of the detected X-rays. Calculations based on the material structure and measured at 5.9 keV found the design to be compatible with the 4% rms, the requirement for transmission homogeneity at 6 keV.

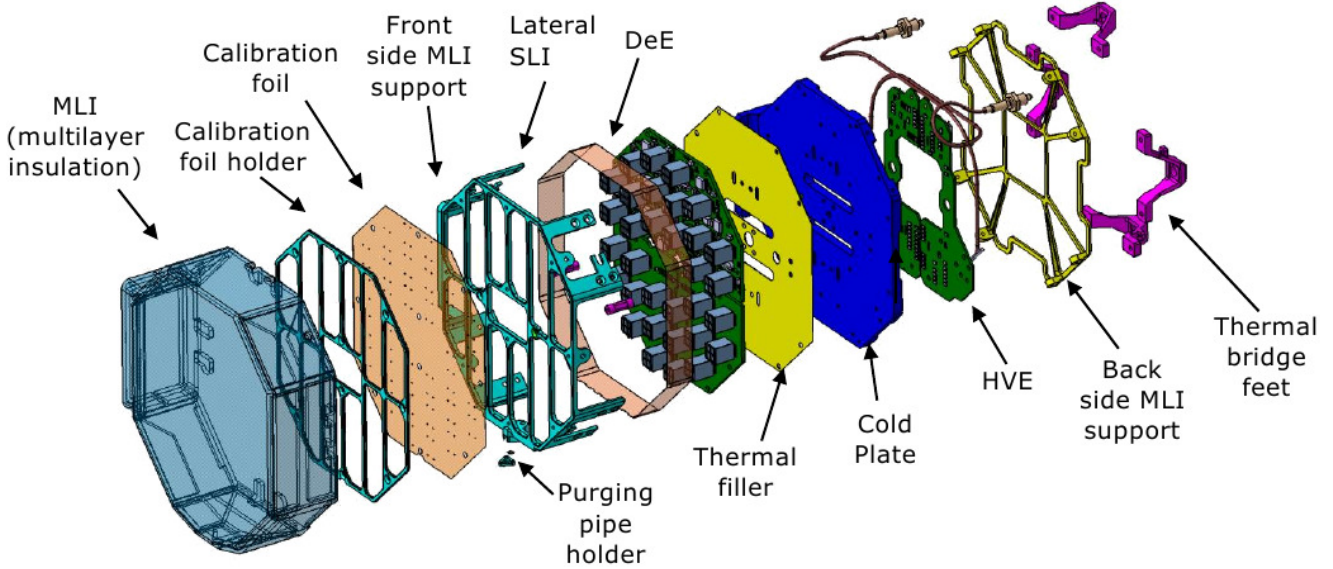


**Fig. 14.** Exploded view of the cold unit. The cold plate (blue) is connected to the spacecraft radiator, the front-end electronics are mounted on this plate. This is enclosed by multi-layer insulation and supported by Vetronite thermal bridge feet (pink).

#### 5.4. Energy calibration sources

Imaging in a given energy range is based on the relative count rates among different detectors and pixels. In the presence of steep flare spectra, the count rate ratios (and hence the imaging) would be potentially compromised if the relative energy calibration were not accurately known (goal: 100 eV rms). This goal is addressed by continuously illuminating each pixel with X-rays from  $^{133}\text{Ba}$  radioactive sources inside the cold unit. For each pixel, ground analysis of the resulting spectra determines the ADC channels corresponding to two peaks of known energy. The results are then uploaded to STIX for real-time application (see Sect. 7.3.1.).

Taking into account its 10.5 year half-life, the source activity that is necessary to obtain such a calibration should be sufficient to overcome background while not unduly degrading the instrument sensitivity to weak flares. Prelaunch estimates of the background were based on Geant4 Monte-Carlo studies, which indicated that the background will probably be dominated by direct observation of the well-known diffuse cosmic X-rays, with a smaller contribution from partially-shielded time-variable charged particles. This led to the selection of a total source activity of 4.5 kBq, distributed over 128 individual dots to ensure comparable illumination of all pixels.

Ground tests confirmed the feasibility of this process using spectral measurements with the internal calibration source in the fully assembled DEM during the final thermal-vacuum testing campaign of STIX. Results from this test are shown in Fig. 15.

#### 5.5. Sensor degradation

##### 5.5.1. Polarization effects

Schottky CdTe detectors are subject to a polarization effect, a change of the internal electric field as a function of time under bias due to varying space charge (Cola & Farella 2009; Meuris et al. 2011). In general this results in a leakage current increasing with time, decreasing resolution and reduction of the sensitive volume. The sensor can be restored to the pre-polarized state by a relatively brief removal of the applied bias. Measurements at a

temperature of  $+4^\circ\text{C}$  and 200 V bias indicate a typical time scale of about half a day for doubling the FWHM. Setting the bias to 0 V for two minutes completely restored the initial performance. The polarization interval increases with decreasing temperature and is about one month at the nominal operating temperature of  $-20^\circ\text{C}$ . Short bias resets on a daily time scale are foreseen to be executed automatically in flight. The reduction in live-time due to this effect is thus negligible.

CdTe is also subject to a rate-dependent polarization effect. However, this sets in at rates in the range of 1 to  $10 \times 10^6 \text{ mm}^{-2} \text{ s}^{-1}$ , and so may only become relevant for low-energy spatially-integrated spectroscopy using the (unattenuated) BKG detector during events that exceed GOES Class X10.

##### 5.5.2. Radiation damage to detectors

Many different components on the spacecraft and payload will suffer radiation damage during the 10-year mission. Of particular importance to STIX is the degradation of its CdTe sensors. This is due to displacement damage in the crystal lattice from non-ionizing energy loss of energetic protons (Eisen et al. 2002). The dominant source of this degradation is the episodic short-lived high fluences of those particles during solar proton events, as opposed to the continuous exposure to galactic cosmic rays<sup>8</sup>. Radiation damage occurs therefore not linearly in time, but it is strongly solar cycle dependent.

To estimate the degradation that has to be expected, CdTe crystals from the production run were irradiated by 50 MeV protons with a fluence of  $1.6 \times 10^{11} \text{ cm}^{-2}$  at the Proton Irradiation Facility of the Paul Scherrer Institute. This results in about the same non-ionizing energy deposition as the actual proton spectrum. The range of protons with this energy in CdTe is 6.7 mm, so an approximately homogeneous damage distribution is obtained in the 1 mm thick material<sup>9</sup>. In the test, the total fluence was accumulated over a period of 20 h with a flux of

<sup>8</sup> See Sect. 4 of TEC-EES-03-034/JS, Solar Orbiter Environmental Specification, Issue 3R1 (13 June 2012), for the expected mission-integrated proton fluence spectrum.

<sup>9</sup> The neutron fluence at the location of the CdTe crystals was estimated through a Geant4 simulation to be negligibly small.

$2.2 \times 10^6 \text{ s}^{-1} \text{ cm}^{-2}$ . Ten unbiased CdTe crystals were irradiated at room temperature<sup>10</sup>. To obtain degradation data as a function of exposure, two detectors were removed after each 20% fluence step.

After about one week, the crystals were evaluated for leakage current and spectral performance (energy calibration and resolution). The observed evolution with fluence of the FWHM at 31 keV is shown in Fig. 16. The behavior of the resolution at 81 keV was similar to the low energy line, rising roughly linearly to an average of 12 keV at 100% fluence, with a large spread among pixels. In practice, a continuous change in the in-flight spectral performance and energy calibration is partly mitigated since the calibration and resolution are monitored on board with a radioactive source so that the analysis and FSW parameters can be updated accordingly. Retests of the irradiated crystals after 3 months storage at room temperature showed that annealing would not be sufficiently beneficial to be useful in the Solar Orbiter context.

### 5.6. Instrument data processing unit

Direct digital control of STIX components is via a single FPGA with a 100 MHz main clock, located in the IDPU (Instrument Data Processing Unit). It connects to the front-end and back-end electronics and the power supplies, acquires house keeping data, interfaces with various memories, and interfaces with the spacecraft via SpaceWire.

Two nearly identical boards containing the main IDPU components are available in cold redundancy<sup>11</sup>. A switchboard interconnects the two boards and interfaces to the front-end and the Imager electronics.

The flight software runs on a LEON3 Sparc3-type processor with 20 MHz clock frequency, synthesized on the FPGA. The software is divided into two separate parts: the immutable start-up software (SuSW) and the modifiable application software (ASW). Upon application of power to the IDPU, the SuSW is executed automatically. It performs basic power-on health checks and provides boot telemetry to the spacecraft. If no blocking issues are detected, it loads the ASW from Flash memory and transfers control to it. The SuSW also provides the capability to upload new versions of the ASW from ground, either in full or by patching.

The ASW contains all control and science functionality. Its organization and functions are described in Sect. 6.

There are four types of onboard memory:

- 1 MiB of unchangeable EEPROM made up by 8 chips of 128 KByte each. EEPROM is accessible to the FPGA and used to store 3 copies of the Start-up software (SuSW), which includes the basic software drivers (BSW). Each SuSW copy is stored in a separate chip to allow for protection of the SuSW by majority voting.

- 2 Mbytes of SRAM, which serves as working memory for the SuSW. When the Application Software (ASW) is loaded, it stores accumulators, lookup tables, etc.

- Two 64 MByte SDRAM chips, one of which serves as working memory for the ASW and the other for the rotating buffer (Fig. 17).

<sup>10</sup> In flight, the detectors will be constantly cooled, but biased only during allocated observation windows. There are no indications, however, that the results would be significantly changed depending on bias or temperature.

<sup>11</sup> The difference between the boards is an identification accessible to the FPGA, indicating if the currently running board is the main or redundant one.

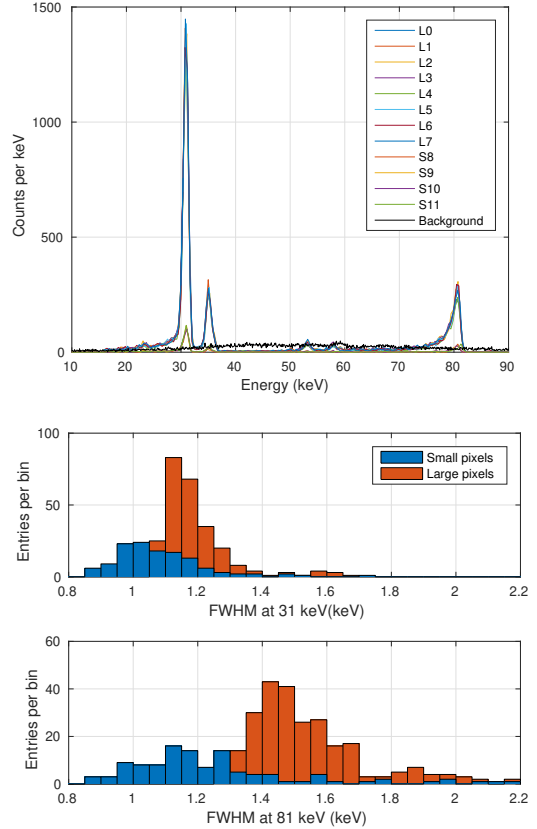


**Fig. 15.** Top: energy spectrum obtained with the  $^{133}\text{Ba}$  internal calibration sources for subcollimator 5. The count rate was  $87 \text{ s}^{-1}$ . The expected background in flight for a large pixel is also shown. Two panels below: FWHM energy resolution for all 384 pixels at 31 keV (middle) and 81 keV (bottom). The better energy resolution of the small pixels can be clearly seen in the figure, resulting mainly from their smaller capacitance. At a shorter shaping time of  $1.78 \mu\text{s}$ , the resolution is worse by about 200 eV.

– 16 GBytes of flash memory, some of which contains multiple copies of the ASW (+BSW), parameter tables, flare list and look-up tables. However, most of the flash is used for the archive and telemetry buffers. All except the ASW are ECC protected.

### 5.7. Power supply unit

The spacecraft provides the PSU with two +28 V lines, one for the main and one for the redundant side (cold redundancy). Commands from the spacecraft select which side of STIX is used. The PSU contains the circuitry for handling the spacecraft High Power Pulse Command (HPC) signal and Bi-level Switch Monitor (BSM) read-back.

All low voltages are generated via windings on a single, main transformer, then regulated and filtered as required. Analog voltage, current, and temperature measurements are passed to the IDPU for digitization. The PSU also contains two high-voltage DC-DC converters to supply the CdTe sensors via the front-end electronics, each converter supplying one half of the sensors without cross-strapping. Both converters are accessible by the main and the redundant side.

The low voltages are divided into essential and non-essential lines. The essential voltages comprise the FPGA and SpaceWire lines, which cannot be switched by STIX itself. In case a severe anomaly is detected, a telemetry report will be sent to the spacecraft, requesting an immediate power down. The non-essential

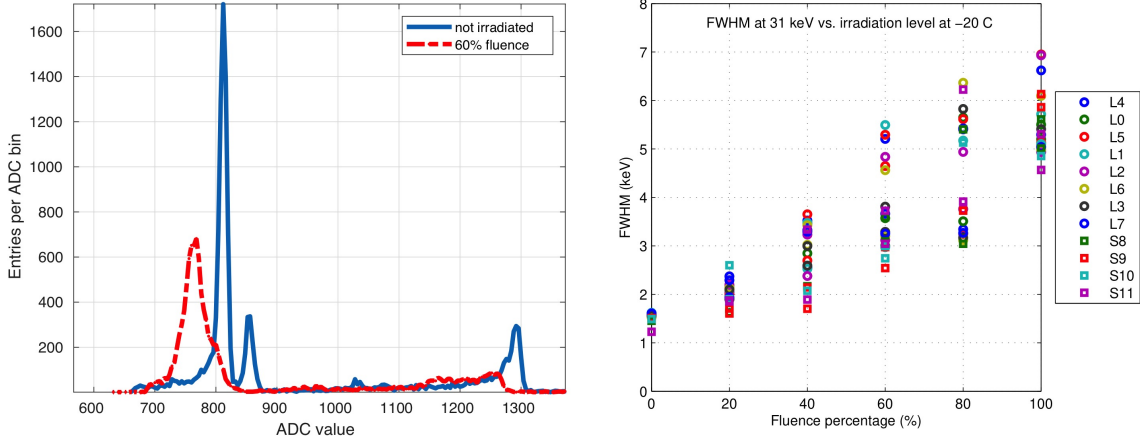


**Fig. 16.** Results from the proton irradiation studies. *Left panel:* spectra before (blue) and after irradiation (red) in ADC counts. *Right figure:* evolution of the FWHM resolution at 31 keV for all 12 pixels as a function of fluence for the eight large (L) and four small (S) pixels. Mission lifetime of ten years corresponds to 100% fluence with the highest radiation damage occurring during solar maximum.

lines supply the detector front-end, the aspect system, the attenuator, and the high-voltage supplies. They are switched under software control and will be disabled in case an anomaly results in a transition to safe mode.

## 6. Onboard data handling

This section describes the onboard handling of the digitized X-ray and aspect data.

The design driver for the IDPU's X-ray data processing is the need to reconcile an input stream of up to 800 000 photons per second ( $\sim 20 \text{ Mbits s}^{-1}$ ) to a telemetry budget of 700 bits per second. This is done by combining rapid FPGA sorting and accumulation of individual events with slower application software that processes the accumulator contents. Figure 17 indicates the overall data flow.

The goal of the FPGA's prompt processing is to sort and sum the input photon stream into accumulators on the basis of their detector ID, pixel ID and detected energy in keV. Application software running on a LEON3 processor then proceeds along three parallel paths:

- a primary path that handles the X-ray imaging and spectroscopy data;
- a quick-look (QL) path that supports the generation of light curves and other products used to monitor the performance of the instrument and to provide a continuous overview of solar activity;
- a calibration path that acquires data needed to establish the energy calibration of each detector/pixel.

### 6.1. Prompt processing

From a digital perspective, the X-ray input to this task consists of an asynchronous stream of 24-bit “photon words”, each of which corresponds to a single detected X-ray, specified by the detector ID (5 bits), pixel ID (4 bits), 3 spare bits, and the 12-bit ADC output which is a linear representation of the detected photon energy.

The first step in handling each photon word is to correct the ADC output for a known weak temperature dependence. This correction is implemented by applying a small detector-, pixel-, and temperature-dependent offset (configurable) to the 12-bit ADC output for each photon. The modified ADC val-

ues are used for subsequent processing where they can be considered to correspond to a common, predetermined reference temperature.

Since it is neither practical nor necessary for the primary and QL paths to retain the full 12-bit energy resolution, the next processing step is to rebin the detected energy for each photon into one of 32 broader “science energy channels”. This is done by the FPGA with a detector- and pixel-dependent, programmable look-up table. The rebinned energy provides 30 energy channels between 4 and 150 keV plus two integral channels for energies above and below these limits. An important rebinning feature is that despite potentially different calibrations, the boundaries that separate the science energy bins are matched in terms of keV among all detectors and pixels. Also, rather than having equal widths, the science energy bin widths are optimized for typical flare energy spectra, with a 1 keV width at lower energies, broadening gradually at higher energies (Fig. 1). Simulations have shown that energy binning on this scale does not significantly degrade spectroscopic analyses.

### 6.2. Primary data path

In the primary data path, each photon word increments one of 12288 double-buffered accumulators (32 energies  $\times$  32 detectors  $\times$  12 pixels). Accumulation continues for an integral number of 0.1 s periods until one of two conditions is met: (1) a preset minimum integration time has been exceeded AND a preset count threshold (within a specified energy range) has also been exceeded; OR 2) a preset maximum integration time is reached. The use of programmable, adaptive integration times enables subsequent data handling to be efficient during solar quiet periods while still supporting high time-resolution during flares. With suitable parameter selection, the option of fixed integration times is also available.

As each integration is completed, the FPGA transfers the contents of the accumulators into a time-tagged rotating buffer. The contents of the rotating buffer are subsequently compacted (partly by eliminating accumulators with zero counts) and stored into 16 GBytes of flash memory. This “archive buffer” can be retained on board for several weeks and provides the input for all subsequent primary analyses. It is important to note that despite the foregoing energy and time binning, the archived data can be generally considered scientifically lossless in the sense that

## STIX On-board Data Flow

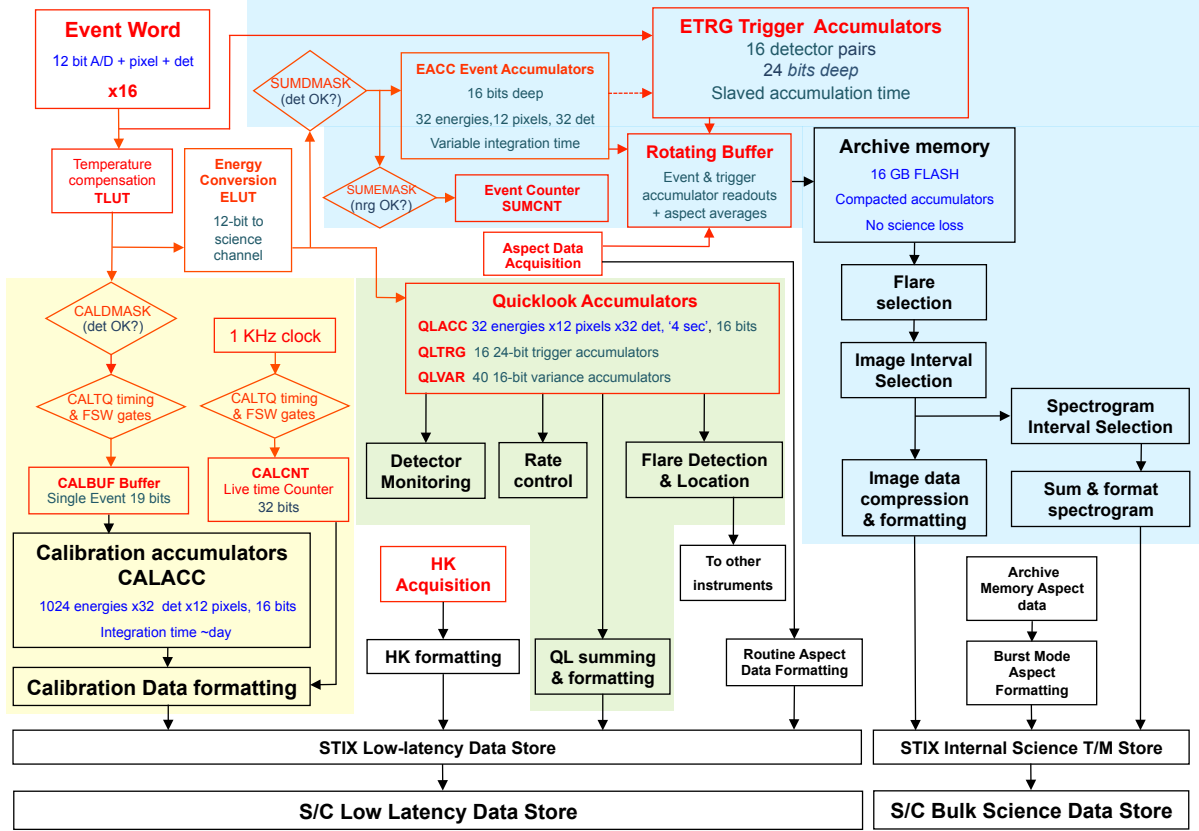


**Fig. 17.** Overview of the onboard data flow. Red boxes indicate FPGA processing; blue background is primary data path; green is the QL data path; yellow is the calibration data path.

higher time- or energy-resolution could not be exploited for statistically significant solar analysis.

In parallel with the photon word handling, one of 16 trigger accumulators is incremented each time a trigger is generated by a “not-busy” detector. Trigger counters accumulate for the same time intervals as the event counters and their output is carried along with event counts in subsequent data handling and analysis steps. Photons that are detected in more than one pixel in a detector pair generate a single trigger but are otherwise excluded from subsequent analysis and do not generate a photon event word. The dead time is digitally the same for all triggers (nominally 12.5 microsec). Therefore the trigger rate alone is sufficient to directly measure the live time for the corresponding detector pair. An important corollary is that all pixels in a single detector share a common live time. This greatly eases the interpretation of intra-detector count rate comparisons which form the basis for imaging.

### 6.3. Quick-look data path

As with the primary data path, the QL data path also begins by feeding the photon words into a (separate) set of 12288 double-buffered accumulators. In this case, the accumulation intervals are fixed (4 s nominal). In most cases the calculation of QL products requires only summing various combinations of the QL accumulator contents. In five cases detailed in subsequent subsections (also see Table 3), more extensive calculations are required. Except as noted, the calculation of QL products must be completed within the 4 s QL-integration time.

#### 6.3.1. Flare detection

The goal here is to detect flares in real time and to provide a rough measure of their intensity. The detection algorithm uses two time sequences of detector-summed counts, corresponding to different energy bands (to support detection of thermal and nonthermal X-rays). For each band, two different averaging times (multi-second and multi-minute) are used to provide sensitivity to both impulsive and gradual events. A flare is deemed detected when current counts in any of the four cases exceeds a preset minimum count rate while representing a significant fractional increase relative to a longer term average. The flare is deemed to have ended when all the triggering count rate(s) fall below a preset fraction of its maximum. The flare status is included in real-time data transmitted to other instruments with an overall 4 to 8 s latency.

#### 6.3.2. Coarse flare location

As discussed in Sect. 4.5, the CFL subcollimator illuminates its detector with a distinctive shadow pattern whose position depends on the flare centroid location relative to the STIX imaging axis. Combining the eight CFL pixel count rates with averages from other detectors, the centroid location is estimated on board in successive 8 s (nominal) intervals by maximizing the correlation of the various count rates with expectations calculated for an array of  $65 \times 65$  potential flare locations. The result is a location digitized to 2 arcmin and included in the data distributed to other instruments in real time.

**Table 3.** Calculation of quick look T/M items.

Item	Calculation	Default parameters	T/M [bits s <sup>-1</sup> ]
Light curves	Sum over pixels, detectors, time, and energy	4 s 5 energy bands	14.2
Background	Sum over BKG pixels, time, and energy	8 s	6.1
Detector spectra	Sum over pixels and time. multiplex detectors	same 5 energy bands 32 s 30 energy bands	8.8
Variance	See Sect. 6.3.5	4 s	2.0
Flare flag and location	See Sect. 6.3.1 See Sect. 6.3.2	1 energy band 8 s	3.0
Flare and T/M management	Not yet implemented	~20 h	0.5
Calibration spectra	Sum over selected spectral regions	32 detectors, 8 pixels, 20 h, 5 spectral ranges	10.0
Contingency			5.4
Total			50.0

To ensure adequate statistics while avoiding potential nonlinear effects at very high count rates, the real-time flare location is calculated only when flare count rates are at intermediate levels. This should not be an issue since once underway, flare centroid locations are typically stable on a 2 arcmin scale.

#### 6.3.3. Detector monitoring

The purpose of this task is to identify malfunctioning detectors that exhibit abnormally high count rates. Although such detectors can increase the volume of T/M and data within the archive buffer, their most serious impacts are that they may provide erroneous input to the QL accumulators and to some onboard decision-making algorithms. Restricted to non-flaring times, the detector monitoring task identifies any detector with count rates that persist at significantly higher levels than those of its peers in either of two preset energy ranges. The offending detector is then flagged in appropriate masks to exclude it from any decision-making role and from QL light curves calculations. More detailed diagnostics, mitigation and restoration are handled after the fact by the ground segment.

The onboard impact of detectors that fail by not providing any output at all is much more benign and so their identification and mitigation is deferred to the ground segment.

#### 6.3.4. Rate control regimes

This task uses detector-summed trigger rates to identify and initiate the most appropriate attenuator and pixel states to maintain viable event rates without unnecessarily sacrificing sensitivity. Details are described in Sect. 6.5.

#### 6.3.5. Variance calculation

To monitor for “bursty” detectors and for significant subsecond time variations in the solar flare flux, a variance measure is calculated and included in the QL data. This is done by accumulating detector-summed counts in a preset energy range into a set of 40 successive 0.1 s time bins. After 4 s have elapsed, a variance measure among the contents of these 40 accumulators is

calculated and transmitted as part of the QL T/M. The conversion to actual variance and evaluation of its statistical significance (if any) is done on the ground.

#### 6.4. Calibration data path

The purpose of the calibration data path is to obtain high-resolution spectral data from the weak onboard <sup>133</sup>Ba X-ray sources (see Sect. 6.3.2). These data provide the input to ground-based spectral fits that determine the gain and offset for each detector and pixel. The onboard spectral accumulation is based on a 10 bit representation of the 12-bit (temperature-compensated) ADC output in the event word. Events are summed into 393 216 accumulators (1024 energies × 32 detectors × 12 pixels) over a commandable multi-hour timescale. To ensure that the <sup>133</sup>Ba spectra are not overwhelmed by solar photons, accumulation is restricted to periods when the Sun is quiet. This determination is made automatically by requiring that no event be accumulated unless a minimum specified time interval (~milliseconds) has elapsed since a previous photon detection. Such a criterion automatically suppresses accumulation during periods of enhanced count rates. To establish the normalization of the resulting spectra, live time is measured using a 1 kHz oscillator whose output is gated and summed over the same times as when an incoming event could be accumulated.

After the X-ray accumulation is completed, the resulting spectra can be flexibly truncated and/or averaged and the results included in the QL telemetry.

#### 6.5. High rate handling

STIX is exposed to solar photon fluxes that can range from background levels of  $\sim 10^2$  photons s<sup>-1</sup> to over  $\sim 10^{10}$  photons s<sup>-1</sup> for flares above GOES X10. Such a range implies that the detector and data handling limits of  $\sim 800\,000$  photons s<sup>-1</sup> can certainly be exceeded. Several strategies, outlined below, are applied successively to avoid exceeding the count rate limits.

- Each individual detector can analyze up to  $\sim 20\,000$  events s<sup>-1</sup> by relying on live time measurements (up to  $\sim 50\%$ ) to renormalize the observed count rate data. This supports the basic capability of  $\sim 800\,000$  photons s<sup>-1</sup>.

– At potentially higher count rate levels the movable aluminum attenuator (Sect. 5.2) can be inserted in front of the detectors to reduce the intense low-energy photon rate from flares by a factor of  $\sim 10^2$  while still transmitting almost all the high-energy photons. Renormalization as a function of energy is performed during post-analysis.

– At still higher levels, individual pixels can be temporarily disabled (top and/or bottom rows of large pixels) to reduce the effective detector area (and count rates) in 2 additional steps to provide an additional factor of up to 20.

– An additional option (“pixel cycling”) is available that cyclically enables selected individual pixels or pixel pairs on a short timescale so that only one or two pixels in each detector are active at any one time. While still rapidly sampling the complete Moire pattern, this provides an additional factor of 2 or 4 reduction in instantaneous rates, thereby adding additional dynamic range.

Overall, the combination of attenuator insertion, pixel disabling and pixel-cycling can reduce the rate of analyzed events by a factor of up to  $\sim 10^4$ . Taken together, these strategies imply eight specific instrument configurations or “rate control regimes” (RCRs) that are autonomously invoked and relaxed sequentially under software control. There is a latency of 4 to 12 s between the occurrence of an enhanced rate and its mitigation by changing the RCR.

## 6.6. Data selection and autonomy

As the foregoing discussion suggests, there are three important distinctions between the QL and primary X-ray data handling: first, the QL data represent only spatially-integrated data; second, the QL data are acquired and transmitted with fixed parameters such as a 4 s cadence; third, there is no provision for onboard QL data selection. In contrast, the much more voluminous primary data can only be transmitted on a highly selective (flare-associated) basis, albeit with a wide range of choices for time- and energy- resolution and coverage. These choices can be optimized to match the dynamic characteristics of the flare in question. Thus by limiting consideration to flare intervals only, and by optimizing time and energy range and resolution for the individual flare, the scientific efficiency of imaging and spectroscopic data telemetry can be greatly enhanced.

There are two approaches to selecting the time- and energy-resolution and range for the bulk spectroscopic and imaging data. The first approach relies on the ground segment to select parameters for the downlink of flare T/M. This selection can be based on the QL light curves in 5 different energy bands which together provide a robust indication of flare timing, intensity and spectral properties. The ground segment can use this to choose optimized time range, energy range, and resolution for different phases of the flare, predict the resulting T/M volume and upload corresponding analysis requests. The onboard software then applies these parameters to the data stored in the archive buffer. This option is viable because the latency of the QL data (up to 24 h) is much shorter than the multi-week longevity of the archive buffer. This provides time for the ground segment to make selections and upload parameters and for the FSW to process the data. Since each ground system request result in a predictable telemetry volume, the STIX ground system is responsible for complying with T/M corridor restrictions on the data rate.

There are three downsides to this approach to data selection: first, the selections and choices are a labor-intensive activity; second, selections must be made and satisfied before the onboard

archive is overwritten and so that the choices must be made in a timely fashion; third, there is an additional operational latency of at least a few days between flare occurrence and the transmission of the requested X-ray imaging and spectroscopic data.

With the second approach (“autonomy”), the FSW uses the output of the onboard flare detection algorithm to identify relevant time ranges. It then uses automatic, parametrized algorithms to optimize the time and energy resolution for imaging and spectroscopic data for inclusion in bulk T/M. As of this writing, this option has not yet been fully implemented. When using autonomy, the QL telemetry (Table 3) will include flare and telemetry management information to show the analysis status of recent events.

## 6.7. Imaging data compression

For preparing the bulk science telemetry, the data for each specified time and energy bin (termed one “image”) are compressed to one of four user-chosen data compression (DC) levels. The different DC levels provide the ability to tradeoff telemetry volume for redundancy in the downloaded bulk science data. (Except for the self-calibration benefits, the choice has no direct effect on image quality.) The four available options are:

– Data Compression Level 0: This data compression level downlinks the compacted, unaveraged accumulator contents within a specified time interval in the archive buffer. This is very inefficient and should be used only for diagnostics.

– Data Compression Level 1: For each specified pixel and detector, counts are summed within each requested time/energy bin. This data set retains the full inherent redundancy which can be used for self-calibration (Sect. 7.3.3). For perspective, with DC Level 1 compression, the STIX baseline T/M allocation is sufficient to transmit up to  $\sim 10^3$  user-specified images per hour, each corresponding to a well-defined time/energy bin.

– Data Compression Level 2: This is the same as DC level 1, except that instead of individual pixels, counts are also summed over specified pixel combinations. This can save up to  $\sim 50\%$  of the T/M compared to level 1, but it does discard much of the self-calibration information and does preclude some types of instrument response corrections.

– Data Compression Level 3: For each time/energy bin, specified combination of pixels and detectors, counts are summed and/or differenced for inclusion in T/M. The resulting T/M can be interpreted directly as (uncalibrated) visibilities. This saves an additional  $\sim 20\%$  of T/M compared to DC Level 2. However, it contains relatively little information that can be used for self-calibration.

No image reconstruction is done on board. Instead, for any of these compression options, the detector data for a time/energy interval can be used on the ground to calculate a set of calibrated visibilities. Ground-based image reconstruction then yields a corresponding image. Such images can be interpreted directly, combined to form a temporal “movie” or to obtain feature-dependent spectra either by “image stacking” or directly from the visibilities themselves using regularization techniques (Piana et al. 2007). Additional insights can be obtained from time, detector and spectral comparisons of the amplitudes and/or phases of the visibilities themselves.

As with imaging data, users can also specify time/energy range and resolution for spatially-summed flare spectroscopy data. Since its data volume is relatively modest, finer time/energy bins can be chosen and only one option for data compression is needed. In this case an individual datum corresponds to detector- and pixel-summed counts within the specified time/energy bin.

For organizational and implementation purposes this can be considered as DC level 4.

### 6.7.1. Aspect data handling

Aspect data are included in the telemetry in two forms: first, regular aspect is included in the housekeeping telemetry on a quasi-continuous basis at low (64 s) time resolution, a cadence that is suitable for periods of stable pointing; second, burst mode aspect is included in bulk science telemetry only upon post-facto request by the ground segment which specifies the time interval and cadence (16 ms to 32 s). This option is intended to provide high rate aspect data for periods when the pointing is varying. The aspect data to support post-facto burst mode aspect selections are stored within the archive buffer with a multi-week longevity similar to its X-ray counterpart.

To generate aspect data, the analog output of each active area of the photodiode is digitized at 1000 Hz by a pair of multiplexed 12-bit A/D converters. For each active area, 16 successive outputs are summed into a 16-bit word at a 62.5 Hz rate which is stored in the archive buffer to provide the input for the optional post-facto burst-mode aspect telemetry.

In parallel, the 62.5 Hz stream of aspect values are sampled every 4 s. For each active area, 16 such samples are averaged every 64 s and the averages included in the housekeeping telemetry. This regular aspect data requires about 1 bit s<sup>-1</sup> of telemetry.

### 6.7.2. Integer compression

In addition to the aforementioned processing, all individual values for X-ray count and trigger sums in the QL and bulk science T/M are compressed to 8 bits from their multi-byte internal representations. This integer compression uses a quasi-floating-point format (with parametrization appropriate for each data type) whose range can accommodate maximum realistic expectations. Low values are represented exactly; compression errors for larger values correspond to a fixed fraction (~1.5–~3% rms) of the uncompressed value. Ground decompression is based on lookup tables. Except for X-ray and trigger telemetry values, integer compression is not invoked for any other onboard data handling. In some cases, the use of compression should be considered in evaluating the statistical significance of results.

## 7. Operations, data products, and analysis

This section provides an introduction to STIX instrument operations, calibration, data products, and science analysis, including the interactions among STIX flight hardware, flight software, and the ground segment.

### 7.1. Operations

The STIX instrument has provision for 6 operating modes:

- OFF: Totally unpowered.
- BOOT: Defines the process of transitioning from OFF to SAFE.
- SAFE: The Low Voltage Power Supply but not the High Voltage Power Supply is powered. Only HK data are generated.
- CONFIGURATION: A non-observing mode for updating parameters.
- MAINTENANCE: Used primarily for diagnostics.
- NOMINAL: Normal data acquisition.

A simplified but typical operational cycle would then consist of:

- Transition from OFF, through BOOT and into SAFE mode, loading the ASW and current parameters from Flash memory.
- Optionally go into MAINTENANCE mode as needed to address any non-routine issues.
- Go into CONFIGURATION mode to receive TCs, update observing and calibration parameters as needed, and receive bulk science data requests (if any) for previously observed flares.
- Go into NOMINAL mode to acquire X-ray data while processing bulk science data requests in the background.
- Revert to SAFE mode when observing is completed.
- If necessary, transition to OFF.

Notably absent is provision to adapt the data acquisition to upcoming joint observing campaigns or to solar activity. STIX basically observes in a single mode, adapting in real time to varying solar flux levels. Optimization for the current science campaign is done post-facto through the specification of data selection and analysis parameters. Further flexibility is provided by the ability to choose time and energy coverage and resolution, image field of view and resolution, etc. after the fact during data analysis in response to the characteristics of the flare itself and to specific science objectives. This latter capability is possible because the fundamental observables are visibilities which can be combined linearly in energy and/or time (see Sect. 4.2). The data analysis software fully supports this flexibility.

### 7.2. Implication of telemetry structure

The STIX QL and bulk science telemetry takes the form of many different packet types, each associated with a different type of data. To ensure efficient use of T/M rates, the time coverage of different packet types range considerably, from a few tens of seconds to tens of hours. This implies that at any given time, the epoch of the latest data download will differ among types. While this will be reconciled in the data bases with subsequent T/M passes, users intent on viewing the most recent data may wish to take this into consideration.

An exception to this is the periodic HK data in which all parameters are reported in the same packet at a fixed 64 s cadence.

### 7.3. Calibration and self-calibration

Also absent from the observing modes are any special provisions for calibration. Although aspect and routine energy and alignment calibrations are expected to be provided by the STIX team, we summarize here some elements of the energy and alignment calibration and self-calibration.

#### 7.3.1. Energy calibration

STIX onboard data handling is based on “science energy channels” (Sect. 6.1) whose boundaries in keV must be well-matched among all detectors and pixels. Therefore it is essential that a current energy calibration be maintained on board to support the real-time conversions from native (ADC) channels to science energy channels (keV). This calibration is expected to drift not only over mission timescales as the detectors age and accumulate radiation damage but also on shorter timescales as the detector temperature changes. While the latter is addressed during real-time FPGA processing (Sect. 6.1), the strategy to mitigate long-term drifts employs on-board <sup>133</sup>Ba calibration sources to accumulate spectra over a multi-hour period. Two prominent

lines in these spectra can be fit on the ground to yield the energy calibration gain and offset for each detector/pixel. Due to the good response linearity of these detectors, fitting two lines is sufficient to define the calibration. These parameters are then uploaded so that timely calibration information is available to the FPGA to support the conversion to keV-specified bins. While this can be a continuous process so long as STIX is observing, a significant ( $>1$  week) gap in observing may require operations in NOMINAL mode to acquire, process and upload calibration information prior to restarting joint solar observations. The routine operational latency between acquiring and uploading calibration data is expected to be a few days.

### 7.3.2. Energy self-calibration

For after-the-fact verification that the calibration parameters for all detectors/pixels have indeed been matched, ground analysis can exploit the fact that after calibration, the sum over any set of four phased pixels (A, B, C, D in Fig. 6) should be independent of source morphology. When corrected for live time and grid transmission (Fig. 3), each set functions as an independent, calibrated spatially-integrating spectrometer. There are 90 such sets of independent measurements for any time interval in any flare (top, bottom and small pixels for each of the 30 Fourier subcollimators). Given the steep rise and fall in such spectra (Fig. 1), relative energy shifts between them should provide a sensitive confirmation of relative errors in energy calibration gain and offset. Some insights into inter-pixel calibration can also be obtained from the cross-check noted in Fig. 6 and as well from statistical comparisons of visibilities within and among flares.

Pulse pileup is a detrimental effect at high rates that is due to multiple photons interacting in a given detector pixel within its charge-collection integration time. Although pulse pileup is not expected to be significant in STIX, its absence can be confirmed by comparisons of spectra formed from the large and small pixels. Since the latter are eight times smaller than the former, any pileup artifacts in their spectra should be reduced by a similar factor.

### 7.3.3. Alignment self-calibration

Although the relative orientation and displacement of the front grid, rear grid, and detectors were carefully determined during instrument assembly, one cannot rule out the possibility of changes during the mission due to thermo-elastic deformations. However, the metrology can be monitored in flight using flare data redundancies such as listed below:

- The relative twist orientation between the front and rear grids can affect the visibility amplitude calibration. For a known subset of subcollimators, such misalignment also results in readily detectable phase shifts among the 3 redundant visibility measurements for each such subcollimator (top row, bottom row, and small pixels). This provides the basis for sensitive monitoring (and subsequent mitigation) of the relative orientation of the front and rear grids.

- The orientation of the individual detectors relative to the grids can be determined since each detector makes three independent measurements of a visibility, using the top and bottom rows of large pixels, and the set of four small pixels. Errors in the orientation of the detector are manifest as systematic phase shifts among the resulting three visibility measurements. The phase shifts should be similar for all flares, energies and times.

- The relative displacement (parallel to the mounting panel and perpendicular to the incident X-rays) of the imager and the

detector assembly has a direct effect on the measurement of visibility phase. To monitor this, the subcollimators have been divided into two comparable sets (in terms of their  $uv$  coverage). In one set, a given mechanical displacement increases the measured phases; in the other set, the same displacement decreases the phases. Images, independently reconstructed from each set will be best-matched when the correct relative displacement is used.

Note that corrections for moderate alignment errors can be made post facto during analysis. Unlike conventional optics, such errors do not affect image resolution or quality except for a modest impact on statistics. STIX imaging has only a weak dependence on the separation of grids and detectors.

## 7.4. Data products

The STIX ground segment provides several levels of science data products to support a range of science analyses performed with varying degrees of calibration, continuity, and convenience. The science-related products (but not the engineering or non-routine diagnostic outputs) are now discussed.

### 7.4.1. Low latency pipeline

The mission's low-latency pipeline supports QL-based multi-instrument displays at the SOC to support planning activities (Sanchez et al., in prep.). The STIX input to this process is primarily spatially-integrated light curves with 4 s time resolution in 5 broad energy bands (two thermal, two nonthermal and one intermediate). In addition, for the more intense flares identified on board, there are preliminary estimates of the event location (digitized to 2 arcmin) as well as very preliminary estimates of flare X-ray spectral parameters.

This input is intended to provide indications of the timing and significance of solar flare activity as seen from the Solar Orbiter vantage point to support short-term mission planning. It should *not* be used for science analyses; the better calibrated Level 2 data products should be used instead (see Table 4).

### 7.4.2. Level 1 data products

Ground-generated Level 1 data products, promptly produced by the instrument team, represent the raw T/M, converted to FITS format with only basic formatting and units applied. This level of data serves primarily as more convenient time-ordered machine input to subsequent processing steps.

## 7.5. Level 2 data products

There are two classes of Level 2 data products. They differ in that the first is based exclusively on low latency T/M and so represents a complete systematic record of STIX observations. The science-related subset of these products is detailed in Table 4. They will be promptly produced by the instrument team and can be considered suitable for routine scientific interpretation. The light curve and flare locations in the Level 2 data have improved calibration and so effectively replace the corresponding information in the LL Pipeline. Note that there is no imaging information in this subset.

The second class of Level 2 data products is primarily derived from bulk science T/M, which is generated in response to ground-segment (or automated) data requests. As a result, they do not represent a continuous record of solar activity and may not be available until well after the event occurs. Details

**Table 4.** Level 2 QL-based data products.

Item	Coverage	Time resolution	Energy resolution	Spatial	Calibration level	Units	FORMAT
Light curves	Continuous <sup>(*)</sup>	4 s	5 bands within 4–150 keV	Integrated	Diagonal elements only	ph cm <sup>-2</sup> s <sup>-1</sup>	FITS PNG
Background	Continuous <sup>(*)</sup>	16 s	Same 5 bands	n/a	Live time only	cts cm <sup>-2</sup> s <sup>-1</sup> and ph cm <sup>-2</sup> s <sup>(**)</sup>	FITS PNG
Calibration spectra ( <sup>133</sup> Ba)	During solar quiet periods	~1 day	~0.4 keV in selected bands	Individual detector pixels	Live time only	cts	FITS PNG
Aspect solution	Occasional	~days	n/a	<3 arcsec	Offset from s/c reference axis	arcsec	FITS PNG
Flare list	Continuous <sup>(*)</sup>	Start, end, and peak times	n/a	Approximate location (~1 arcmin)	Various flags	n/a	FITS ascii

**Notes.** <sup>(\*)</sup>If STIX is powered on in nominal mode. <sup>(\*\*)</sup>Equivalent photon flux yielding the same background count rate.

**Table 5.** Level 2 data products.

Item	Coverage	Time resolution	Energy resolution	Spatial	Calibration	Units	FORMAT
Spectrograms	Ground-selected flares only	Ground-selected uniform ~1 to 100 s	Ground-selected up to 30 channels	Integrated	Diagonal elements, grid response, live time	2-D plots flux vs t, E	FITS PNG
Spectra	Ground-selected, flares only	Match to spectrogram columns	Match to spectrogram rows	Integrated	Similar to spectrograms	ph cm <sup>-2</sup> s	FITS PNG
Light curves	Ground-selected, flares only	Match to spectrogram rows	Match to spectrogram columns	Integrated	Similar to spectrograms	ph cm <sup>-2</sup> s	FITS PNG
Visibilities	Ground-selected flares only	Ground-selected nonuniform ~1 to 1000 s	Ground-selected up to 30 channels	30 visibilities	Corrected for live time, diagonal energy response, grid response, metrology	ph cm <sup>-2</sup> s	FITS PNG
Images	Ground-selected flares only	Match to single or combined visibilities ~1 to 1000 s	Match to single or combined visibilities	Full-disk coverage up to 360 × 360 arcsec FOV 7 arcsec resolution	Corrected for live time, diagonal energy response, grid response, metrology	ph cm <sup>-2</sup> s	FITS PNG

are shown in Table 5. The database includes the current best estimate of calibrated imaging and spectral results, made with nominal time and energy resolution. As the calibration improves, the contents of this database may be occasionally updated. The Level 2 data products will be produced by the instrument team and are fully useable for scientific interpretation. Note, however, that their time and/or energy resolution may not be optimum for a given application.

The Level 3 data products shown in Table 6 are derived from the Level 2 database and so reflect the calibration state of the Level 2 data products. These can be used for scientific analyses.

#### 7.6. Use of STIX data products

The products outlined in the tables are intended to meet the needs of a diverse user community. The Level 2 and Level 3

**Table 6.** Level 3 data products.

Item	Coverage	Time resolution	Energy resolution	Spatial	Units	FORMAT
Spatial movies Flux(x,y) vs time	Selected flares	Matches available L2 images ~1 to 100 s	Matches available images	~5 arcsec pixels	ph arcsec <sup>-2</sup> cm <sup>-2</sup> s <sup>-1</sup>	FITS MPEG
Spectral movies Flux/energy vs time	Selected flares and flare features	Matches available L2 spectra ~1 to 1000 s	Matches available spectra	Spatially integrated or feature based	ph cm <sup>-2</sup> s <sup>-1</sup>	FITS MPEG
Nonthermal electron spectra	Selected flares	Single or combined L2 flare spectra ~1 to 1000 s	Matches available spectra	Spatially integrated	Electrons keV <sup>-1</sup> s <sup>-1</sup>	FITS PNG

products can be accessed in the form of movies, images, plots, and other displays. The corresponding digital data are also available in machine-readable form for further optimization, analysis or display by the user. Browser access to these products does not require specific knowledge of either the STIX hardware or software. However, their use is constrained by the fact that the parameters (e.g., time, energy resolution) have been predetermined and may therefore not fully meet the user's needs.

As a result, these databases will be supplemented by an IDL software suite, designed and documented to support users who would prefer to choose their own analysis parameters. With basic knowledge of the instrument, they can generate the customized output either by the remote use of the STIX computing facility or by installing the IDL software at their own site.

Finally, experienced users who want to extend their analysis beyond the routine level can install the software at their own site, extend and modify it as they wish and start their analysis from the Level 1 database, using existing or redetermining calibration parameters as appropriate.

This three-fold strategy of providing the options of direct use of a calibrated data set, re-analysis with provided software tools, or direct access to the level 1 data for custom analyses is based on the approach used successfully for 17 years by the RHESSI mission.

**Acknowledgements.** We thank the many contributors to the STIX project. Without their effort the instrument would not exist. Firstly, this includes the ESA Solar Orbiter project team, and we particularly acknowledge the support provided by Salma Fahmy, Chris Jewell, and Neil Murray. Secondly, we mention the support from our University partners, namely FHNW, PSI, ETH, CBK, University of Wroclaw, CEA, Université Paris-Saclay, the Astronomical Institute, University of Graz, TCD, DIAS, and University of Genova. We also thank all our industrial partners for their dedication and their effort to make STIX happen. In particular, we mention KOEGL Space, Dielsdorf, Ateleris GmbH, Brugg, Art of Technology Zurich, Almotech, Lausanne, 3D plus, France, ESC Aerospace s.r.o., Czech Republic, FoxWorks Aerospace s.r.o., Czech Republic, Astro- und Feinwerktechnik Adlershof GmbH, and Opto Diode Corporation, IOF Jena. We particularly acknowledge Mike Appleby, Jill Klinger, John Moore and Rowan Hildreth of Mikro Systems Inc, Charlottesville for their professionalism and enthusiasm in producing the grids. And last but not least, we thank all the funding agencies that supported STIX: Swiss Space Office, the lead funding agency

for STIX, the Polish National Science Centre (grants 2011/01/M/ST9/06096 and 2015/19/B/ST9/02826), Centre national d'études spatiales (CNES), Commissariat à l'énergie atomique et aux énergies alternatives (CEA), the Czech Ministry of Education (via the PRODEX program), Deutsches Zentrum für Luft- und Raumfahrt (DLR) (grants: 50 OT 0903, 1004, 1204), the Austrian Space Programme and ESA PRODEX, ESA PRODEX, administered in Ireland by Enterprise Ireland, and the Agenzia Spaziale Italiana (ASI) and the Istituto Nazionale di Astrofisica (INAF).

## References

- Auchère, F., Andretta, V., Antonucci, E., et al. 2020, [A&A](#), **642**, A6 (Solar Orbiter SI)
- Brown, J. C. 1971, [Sol. Phys.](#), **18**, 489
- Cola, A., & Farella, I. 2009, [Appl. Phys. Lett.](#), **94**, 102
- Eisen, Y., Evans, L. G., Floyd, S., et al. 2002, [Nucl. Inst. and Meth.](#), **A491**, 176
- Fletcher, L., Dennis, B. R., Hudson, H. S., et al. 2011, [Space Sci. Rev.](#), **159**, 19
- Gan, W., Zhu, C., Deng, Y., et al. 2019, [RAA](#), **19**, 157
- Grimm, O., Bednarzik, M., Birrer, G., et al. 2015, [JINST](#), **10**, C02011
- Hannah, I. G., Christe, S., Krucker, S., et al. 2008, [ApJ](#), **677**, 704
- Holman, G. D., Aschwanden, M. J., Aurass, H., et al. 2011, [Space Sci. Rev.](#), **159**, 107
- Hurford, G. 2013, in *Observing Photons in Space*, ISSI (New York: Springer)
- Kontar, E. P., Brown, J. C., Emslie, A. G., et al. 2011, [Space Sci. Rev.](#), **159**, 301
- Kosugi, T., Makishima, K., Murakami, T., et al. 1991, [Sol. Phys.](#), **136**, 17
- Krucker, S., Christe, S., Glesener, L., et al. 2014, [ApJ](#), **793**, L32
- Lin, R. P., Dennis, B. R., Hurford, G. J., et al. 2002, [Sol. Phys.](#), **210**, 3
- Massa, P., Piana, M., Massone, A. M., et al. 2019, [A&A](#), **624**, A130
- Meuris, A., Limousin, O., & Blondel, C. 2011, [Nucl. Instr. Meth.](#), **A654**, 293
- Meuris, A., Limousin, O., Gevin, O., et al. 2012, [Nucl. Instr. Meth.](#), **A695**, 288
- Michałowska, A., Gevin, O., Lemaire, O., et al. 2010, [Nucl. Sci. Symp. Conf. Rec.](#), **1556**
- Müller, S., St. Cyr, O. C., Zouganelis, I., et al. 2020, [A&A](#), **642**, A1 (Solar Orbiter SI)
- Piana, M., Massone, A. M., Hurford, G. J., et al. 2007, [ApJ](#), **665**, 864
- Rouillard, A. P., Pinto, R. F., Vourlidas, A., et al. 2020, [A&A](#), **642**, A2 (Solar Orbiter SI)
- Walsh, A. P., Horbury, T. S., Maksimovic, M., et al. 2020, [A&A](#), **642**, A5 (Solar Orbiter SI)
- Warmuth, A., Önel, H., & Mann, G. 2020, [Sol. Phys.](#), **295**, 90
- Zouganelis, V., De Groof, A., Walsh, A. P., et al. 2020, [A&A](#), **642**, A3 (Solar Orbiter SI)
- Zhang, Z., Chen, G., Wu, Z., et al. 2019, [RAA](#), **19**, 157